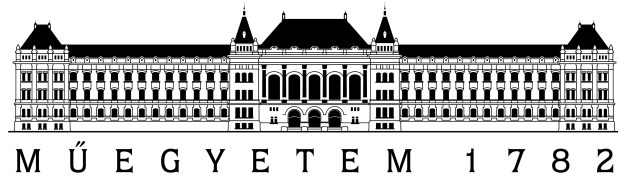


GERGŐ KELLE

Master's Thesis

BUDAPEST UNIVERSITY OF TECHNOLOGY AND ECONOMICS
FACULTY OF MECHANICAL ENGINEERING
DEPARTMENT OF APPLIED MECHANICS





BUDAPEST UNIVERSITY OF TECHNOLOGY AND ECONOMICS
FACULTY OF MECHANICAL ENGINEERING
DEPARTMENT OF APPLIED MECHANICS

GERGŐ KELLE
Master's Thesis

Investigation of the applicability of finite element techniques for
the simulation of Shore hardness tests

Supervisor:

Dr. Szabolcs Berezvai

Assistant Professor

BUDAPEST, 2025.

Copyright © Gergő Kelle, 2025.



Budapest University of Technology and Economics

Faculty of Mechanical Engineering

Department of Applied Mechanics

<http://www.mm.bme.hu/>

FINAL PROJECT ASSIGNMENT

Identification	Name: Kelle Gergő Attila	ID: 75109267879
	Code of the Curriculum: 2N-MW0	Specialisation: 2N-MW0-SM
	Curriculum: Gépészeti modellezés mesterképzési szak	Document ref. number: GEMM:2025-2:2N-MW0:GBBNUL
	Final Project issued by: Műszaki Mechanikai Tanszék	Final exam organised by: Műszaki Mechanikai Tanszék
	Supervisor: Dr. Berezvai Szabolcs, adjunktus	

Project Description	Title	Investigation of the applicability of finite element techniques for the simulation of Shore hardness tests Végelelemes módszerek alkalmazhatóságának vizsgálata Shore-keménységvizsgálatok szimulációjára
	Details	1. Conduct a literature review in the field of Shore hardness tests! 2. Summarize the mechanical behaviour of soft elastomers, summarize the theory of hyperelasticity! 3. Develop several automatic finite element approaches for the numerical analysis of the Shore A hardness tests including CEL classical FEM. 4. Perform parametric FE simulations of Shore hardness tests and evaluate the effect of finite geometries, material nonlinearities and FE techniques! 5. Perform material and Shore tests on selected elastomers and fit a suitable finite strain constitutive model! 6. Compare the experimental and simulation results with the available expressions in the literature! Propose a correction procedure for non-standard measurement arrangements! 7. Summarize the results in English and Hungarian! Prepare a poster presentation of the work!
	Advisor	Advisor's Affiliation: Advisor: ,

Final Exam	1 st subject (group)	2 nd subject (group)	3 rd subject (group)
	ZVEGEMMNWFE Finite Element Analysis	ZVEGEMMNWAM Advanced Mechanics	ZVEGEMMNWCM Continuum Mechanics

Authentication	Handed out: 10 February 2025	Deadline: 23 May 2025	
	Compiled by: Dr. Berezvai Szabolcs Supervisor	Verified by: Dr. Tamás Insperger (signed) Head of Department	Approved by: Dr. Gábor Györke (signed) Vice-Dean
	The undersigned declares that all prerequisites of the Final Project have been fully accomplished. Otherwise, the present assignment for the Final Project is to be considered invalid.		

DECLARATIONS

Declaration of individual work

I, *Gergő Kelle (GBBNUL)*, the undersigned, student of the Budapest University of Technology and Economics hereby declare that the present thesis has been prepared by myself without any unauthorized help or assistance such that only the specified sources (references, tools, etc.) were used. All parts taken from other sources word by word or after rephrasing but with identical meaning were unambiguously identified with explicit reference to the sources utilized.

Budapest, 2025.05.23.

Gergő Kelle

To My Family

The ironic tragedy is that life has to
be lived forward but only makes sense
in reverse.

Søren Kierkegaard

Acknowledgement

First of all, I would like to thank Dr. Szabolcs Berezvai my supervisor for the consultations and advice regarding the progress and possibilities of my thesis. His precision and dedication were a constant source of inspiration to me, because no matter what the adversities involved, we were able to have a pleasant and productive meeting.

This thesis has not merely been an academic requirement to be fulfilled. It marks the closing chapter of my student life a path shaped by countless experiences and connections. Looking back on my years at the university, what stands out most vividly is the people I've had the chance to meet. Over the course of this journey, I've crossed paths with more individuals than I could possibly count each one shaping my experience in some way. It is this vast network of faces, moments, and shared stories that gave true meaning to my time at the BME Faculty of Mechanical Engineering.

At last, I extend my deepest thanks to those who walked this road with me: my friends, the LORD community, the community of GHK, and above all, my family. To my parents: You worked shifts over shifts so that I could have the chance to pursue this path. Your dedication, your quiet strength, and the sacrifices you made gave me the foundation to reach this point, for this reason alone i will always be grateful.

Thank you, Mum.

Budapest, 2025.05.23.

Gergő Kelle

Notations

Latin letters

Notation	Name, comment, value	Dimension
A_0	Initial cross section	mm ²
C_{01}	Material parameter in different models	MPa
C_{10}	Material parameter in different models	MPa
d_0	Max. distance of indenter from panel	mm
d_1	Depth of indentation	mm
D_1	Material compressibility constant	MPa ⁻¹
E	Elastic modulus (Young's modulus)	MPa
F	Load, force	N
\mathbf{F}	Deformation gradient tensor	1
H_A	Shore A hardness	1
h	Specimen height	mm
\mathbf{I}	Identity tensor	1
I_1, I_2, I_3	Scalar invariants of \mathbf{C}	1
J	Volume ratio	1
K	Bulk modulus	MPa
K_A	Correction term	1
L_0	Initial spring length	mm
L_1	Spring length after indentation	mm
P	Nominal stress	MPa
\mathbf{C}	Right Cauchy-Green deformation tensor	1
u	Displacement	mm
W	Strain energy function	MPa
w, r	Specimen width (radius)	mm
x, y	Coordinates	mm

Greek letters

Notation	Name, comment, value	Dimension
α	Material parameter in different models	1
ε	Strain	1
λ	Principal stretch	1
μ_0	Shear modulus	MPa
ν	Poisson's ratio	1
σ	Cauchy stress	MPa

Indices and exponents

Notation	Description
i, j	General indices (integer)

Contents

1	Introduction	1
2	Overview	3
2.1	Introduction to Shore Hardness Testing	3
2.1.1	Standardized Hardness Scales in Elastomer Testing	4
2.1.1.1	International Rubber Hardness Degrees (IRHD)	4
2.1.1.2	Shore Durometer Hardness	5
2.1.2	Shore Durometers	5
2.1.2.1	Historical Context	5
2.1.2.2	Principle of Operation and Indenter Types	5
2.1.3	Shore Durometer Measurement Specifications	8
2.1.4	Correlation Between Shore A Hardness and Elastic Modulus	8
2.1.4.1	Gent's Approximation	8
2.1.4.2	Finite Strain Modeling by Qi et al.	9
2.1.4.3	Summary	10
2.2	Theory of Hyperelasticity	10
2.2.1	Strain Energy Potentials	11
2.2.2	Neo-Hookean Model	12
2.2.3	Ogden Model	12
2.2.3.1	Ogden Model with N=1	13
2.2.3.2	Ogden Model with N=2	13
2.2.4	Mooney-Rivlin Model	14
2.2.5	Derivation of the Uniaxial Stress Expression	14

3 Measurements	17
3.1 Uniaxial Compression Tests	17
3.2 Uniaxial Compression Results	19
3.3 Material Model Fitting	20
3.3.1 Silicone	20
3.3.2 Elastosil	21
3.3.3 Rubber	22
4 FE model development	23
4.1 Model Objectives and Approach	23
4.2 Shore Hardness Calculation from FE Simulation	23
4.3 Geometry and Indenter Setup	29
4.4 Boundary Conditions and Loading	30
4.5 Meshing	31
4.5.1 Mesh Zones and Refinement Strategy	32
4.6 Automation of the Simulation	34
5 Parameter Study	37
5.1 Effect of Geometric and Material Parameters	38
5.2 Correction Method for Non-standard Setups	44
6 Experimental Results and Validation	51
6.1 Introduction	51
7 Summary	57
Összefoglaló	59
Reference	60

1

Introduction

Although Shore hardness testing is widely used in industry and valued for its simplicity, it remains a fundamentally empirical method. This becomes a real challenge when dealing with soft elastomers materials that stretch easily, behave nonlinearly, and sometimes respond differently over time. In such cases, it's hard to draw a clear connection between the measured hardness and the material's actual mechanical properties. Shore A hardness, while convenient, lacks a direct analytical relationship with fundamental material properties such as Young's modulus or compressibility. Because of this, there is growing interest in using simulation methods, particularly finite element (FE) methods, as a more reliable and quantitative way to understand and predict Shore A hardness. These tools offer a deeper, physics-based insight that traditional hardness measurements simply can't provide on their own. In many real-world situations, it's difficult (or even impossible) to prepare Shore A test specimens that satisfies the geometric dimensions defined in ASTM D2240 standards [1]. In practice, engineers often work with what's available, which means hardness is measured on parts that don't follow the ideal shape.

This raises an important question that this thesis sets out to answer: Is it possible to bypass the strict geometric requirements of the standard test by applying a correction method that compensates for differences in specimen shape? This thesis investigates the feasibility of such an approach. Specifically, it examines whether standardized Shore A hardness values can be reliably estimated from non-standard test specimens through the use of simulation-informed correction functions. The methodology is based on implicit quasistatic FE simulations of the Shore A test, using hyperelastic material models (Neo-Hookean and Ogden) calibrated to uniaxial compression data. The simulation workflow is developed in Python and integrated with Abaqus, automating model generation, meshing,

material assignment, loading, and post-processing of the force-displacement data to extract Shore A hardness values.

A systematic parameter study is conducted to explore how the predicted Shore A hardness is influenced by specimen width, height, and material stiffness. These parameters are varied one at a time across a matrix of simulations. The results are analyzed to identify patterns and sensitivities, and to derive a correction model that transforms the measured hardness on non-standard geometries into equivalent standardized Shore A values. The simulations are validated against experimental data. Selected elastomer materials are tested using standard Shore A durometers and uniaxial compression, the latter providing data for material model fitting. This dual experimental-simulation setup ensures that the derived correction methodology is not only theoretically sound, but also practically applicable.

The overarching aim of this thesis is to develop a reliable, generalizable, and simulation-supported framework that extends the utility of Shore hardness testing to non-standard situations, reducing the reliance on idealized specimen geometries and improving the flexibility of mechanical characterization in industrial and research settings. The structure of the thesis and the interrelated simulation and experimental steps are illustrated in Figure 1.1.

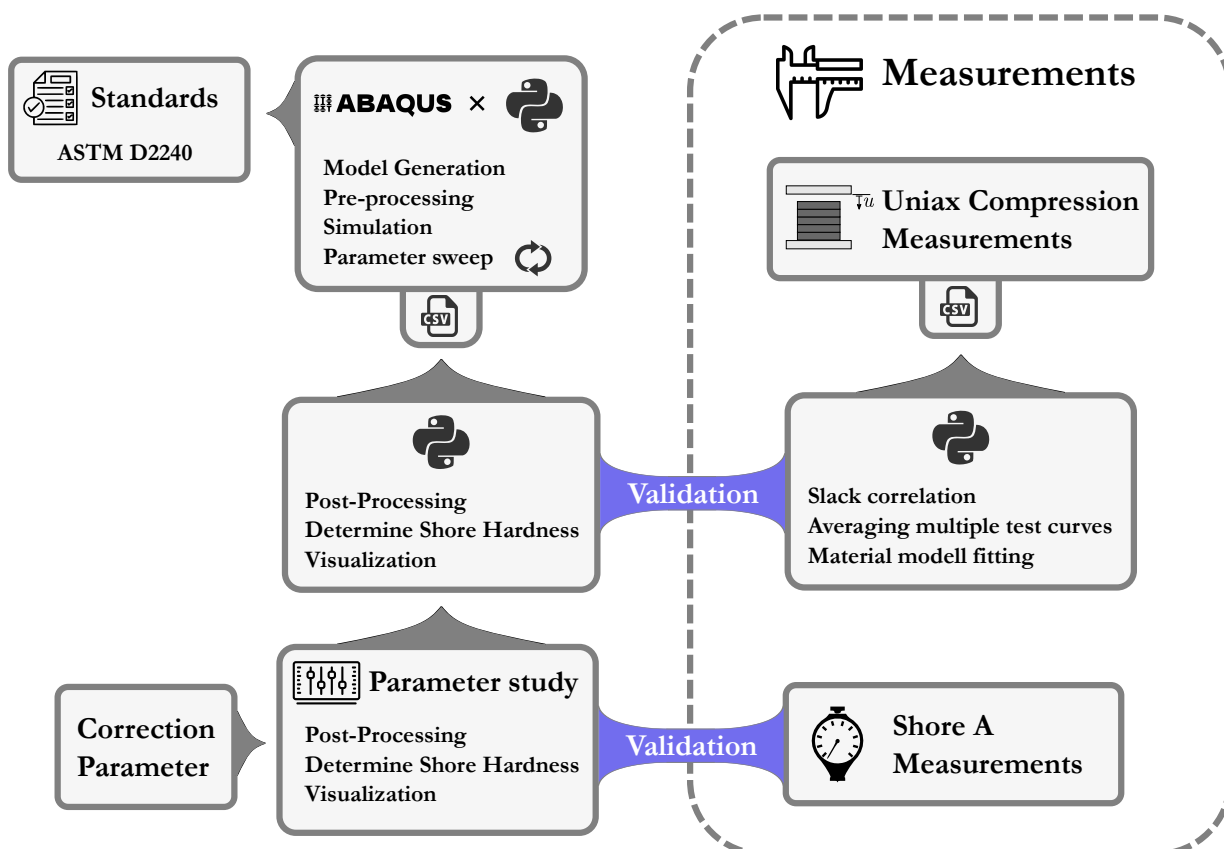


Figure 1.1: Workflow of the thesis structure and simulation process

2

Overview

The goal of this chapter is to give a solid overview of Shore hardness testing and to lay the groundwork for how hyperelastic and elastomeric material models can be applied in this context going forward.

2.1 Introduction to Shore Hardness Testing

Shore hardness testing is one of the go-to methods for quickly assessing how soft or firm a rubber or plastic material is. In practice, it's often used during production or material selection especially for elastomers and softer thermoplastics, because it's simple, doesn't require destructive sampling, and gives results that are easy to compare. The test involves pressing an indenter into the surface, so it's fairly easy and intuitive to use, even outside of a laboratory setup.

The most commonly used standard for this method is the ASTM D2240 [1]. This standard write about how to use the durometer to measure indentation hardness on a given material. Depending on the material's stiffness, different Shore scales are used, like Shore 00 for very soft gels, Shore A for typical rubbers, and Shore D for harder plastics. For the kinds of soft materials used in this project, Shore A is the most relevant based on Figure 2.1.5. Although the Shore hardness value isn't a direct measurement of any single mechanical property, it correlates reasonably well with elastic stiffness and the material's modulus showed in Section 2.1.4. In rubber-like materials, it can also reflect changes in crosslink density from curing, though not as reliably as more specialized lab methods (the crosslinking density wont be subject for my thesis). Depsite its negatives, this hardness

measuring method is useful for quickly assessing whether a material meets certain baseline requirements during processing or inspection.

Even though the test is standardized, it has its flaws. The results can change a lot depending on how the measurement is performed. Things like sample thickness, whether the reading is taken near an edge, how long the indenter is held down, and even small differences in how the durometer is handled can all influence the hardness value. Because of that, Shore hardness is best used to spot larger differences or trends rather than to get precise numbers. Table 2.1.1 outlines the main pros and cons of using a durometer for hardness testing in rubber materials.

Table 2.1.1: Benefits and drawbacks of Shore hardness measurements

Benefits	Drawbacks
Non-destructive and quick method	Poor repeatability due to operator and sample variability
Inexpensive and widely available	Limited precision, especially near sample edges
Applicable on moderately irregular surfaces	Erroneous on highly irregular or thin samples
Easy to use (manual and tabletop options)	

2.1.1 Standardized Hardness Scales in Elastomer Testing

Hardness is a useful parameter in evaluating the mechanical behavior of elastomeric materials. There are two methods which is widespread in industrial use. One of them is the International Rubber Hardness Degrees and the other is the Shore durometer method. Both of them is an international standard, but they differ from each other in case of test mechanics, instrumentation, and interpretation.

2.1.1.1 International Rubber Hardness Degrees (IRHD)

The IRHD method is standardized by ASTM D1415 [2] and ISO 48 [3], which determines hardness by measuring the depth of indentation produced under a deadweight load applied through a hemispherical indenter. The process involves a two-step loading sequence with a minor load to establish a datum point, followed by a major load to induce further indentation. The difference in penetration depths is converted to a hardness value. Although the IRHD scale is intended to correspond qualitatively to the Shore scale, it is inherently nonlinear. This method offers consistent loading conditions and is less sensitive to operator influence, making it more suitable for controlled laboratory environments and more precise measurements.

2.1.1.2 Shore Durometer Hardness

This method is standardized by ASTM D2240 and ISO 48, which uses a spring-loaded indenter. It is mostly used on the field and in factories due to the portability of the equipment. The indenter geometries vary across different Shore types (A, B, C, D, etc.) as shown in Figure 2.1.4. The hardness value is between 0 to 100, and the actual values is derived from the depth of indentation after a standardized dwell time. Despite its convenience and widespread use, the Shore method is more inconsistent, particularly in handheld applications.

2.1.2 Shore Durometers

2.1.2.1 Historical Context

The development of the Shore durometer traces back to the early 20th century. Albert Ferdinand Shore introduced the first commercial device for rubber hardness measurement in 1915. Earlier patents, including one by William F. Shore in 1912, laid the groundwork for spring-loaded indentation-based hardness testing. The instruments evolved to accommodate materials of varying stiffness, with different Shore types denoted by alphabetical progression. This legacy established a foundation for modern portable hardness testing in elastomers.

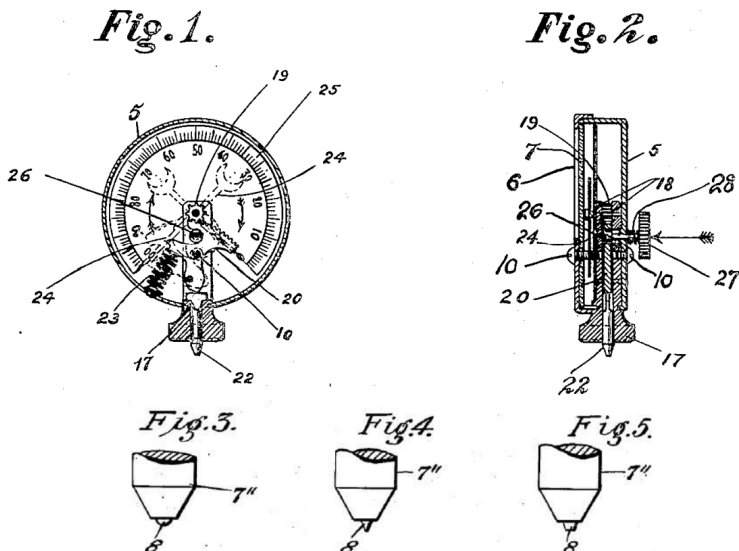


Figure 2.1.1: First drawings of the hardness tester by the Shore-brothers [4]

2.1.2.2 Principle of Operation and Indenter Types

Shore durometers operate on a mechanical principle wherein the depth of an indenter's penetration into a material, under a standardized force, serves as a proxy for its hard-

ness. The indentation depth is inversely proportional to the material's resistance, and the resulting Shore hardness value H is calculated as

$$H = \frac{\Delta L}{d_0} \times 100, \quad (2.1.1)$$

where $\Delta L = L_0 - L_1$ is the displacement of the indenter (from the unloaded to the loaded position), and d_0 is the maximum protrusion of the indenter in the absence of resistance. The physical mechanism behind this indentation process is showed in Figure 2.1.2. When the durometer is not in contact with the specimen (left), the indenter is fully extended to d_0 . Upon pressing the device against the material (right), the indenter retracts as it encounters resistance from the surface, compressing the spring of stiffness k_s . The new equilibrium position defines the measurable displacement ΔL , from which the hardness is derived.

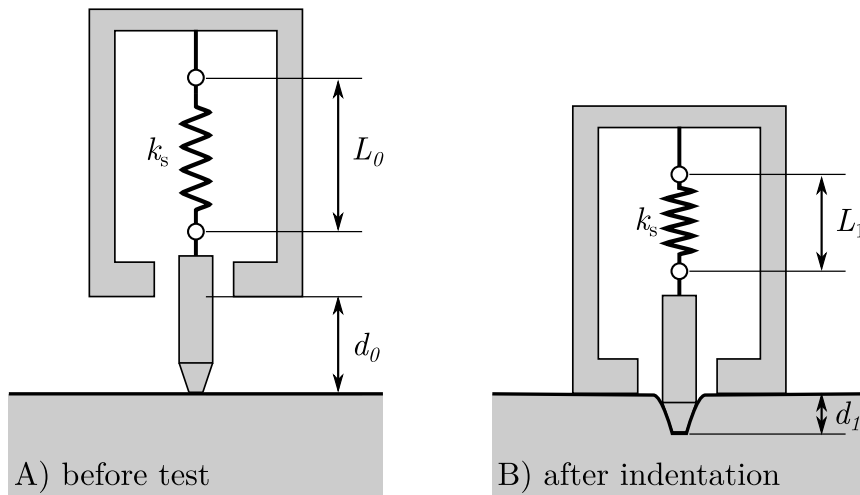


Figure 2.1.2: Schematics of the working mechanism of durometers. (Redrawn from [5])

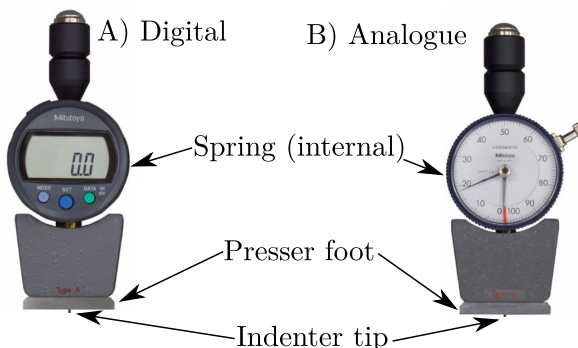


Figure 2.1.3: Schematic layout of a Shore A durometer, highlighting the key components involved in hardness measurement.

A typical Shore durometer, as shown in Figure 2.1.3, consists of a spring-loaded steel indenter, a presser foot to ensure planar contact, a calibrated spring, and an indicating mechanism. These components function in concert to relate spring deformation to material

hardness. The standardized test procedures and instrument configurations are defined under ASTM D2240 and ISO 7619. These standards specify not only the measurement protocol but also a variety of indenter geometries and spring characteristics tailored to different Shore scales (A, B, C, D, O, OO, DO, M). Each Shore type corresponds to a specific indenter geometry and stiffness range, allowing the method to be adapted for materials with widely differing mechanical properties. Figure 2.1.4 presents the indenter profiles used in several Shore scales.

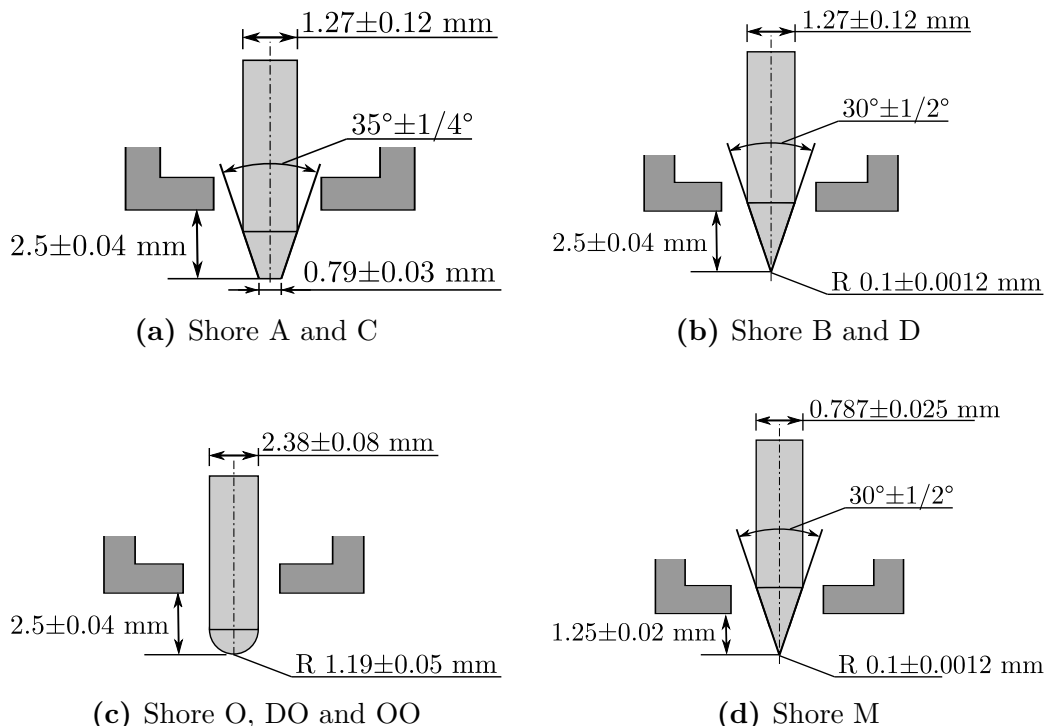


Figure 2.1.4: Comparison of indenter geometries used in various Shore durometer types.

It is important to choose the appropriate Shore scale according to the Figure 2.1.5 which demonstrate how different Shore types overlap in their operational ranges and illustrate their applicability to a variety of elastomeric materials.

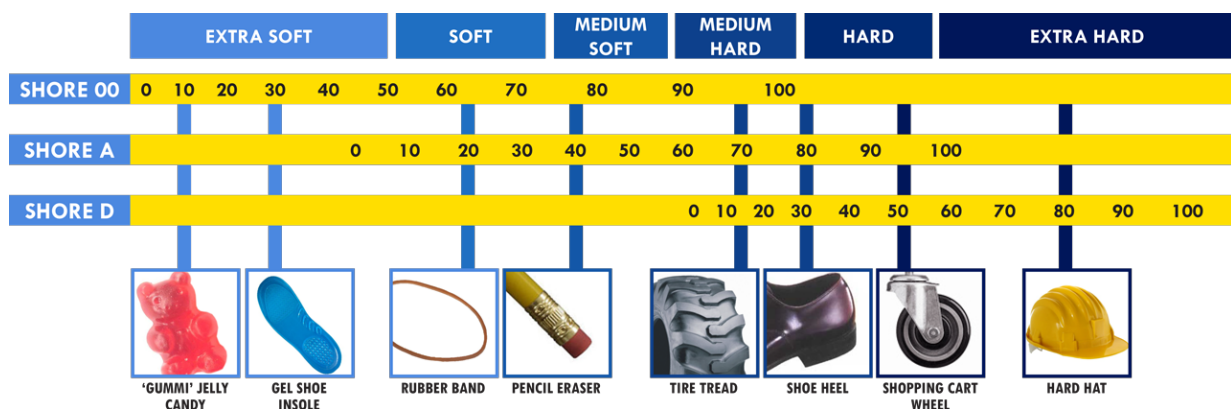


Figure 2.1.5: Shore scales to rubber materials with varying hardness profiles (Source: smooth-on.com).

2.1.3 Shore Durometer Measurement Specifications

ASTM D2240 Requirements

1. Specimen thickness must be at least 6 mm (or 1.25 mm for Shore M).
2. Distance from the measurement point to any edge must be at least 12 mm.
3. The contact surface must be flat and parallel.

Measurement Procedure

Measurements should be taken by applying the durometer vertically onto the specimen, ensuring even contact without shock or lateral motion. Readings are recorded after a 1-second dwell time, with at least five measurements averaged. For improved repeatability, it is advised to use a dedicated (expensive) operating stand. Durometers must be regularly calibrated using reference blocks of known hardness.



Figure 2.1.6: Durometer measurement procedure (Source: kemalmfg.com)

2.1.4 Correlation Between Shore A Hardness and Elastic Modulus

Shore A hardness provides an indirect, yet practical estimate of the elastic modulus of elastomeric materials. Several empirical and semi-empirical models have been proposed to relate hardness to modulus.

2.1.4.1 Gent's Approximation

Gent [6] derived an empirical relationship based on linear elastic theory employing a flat punch approximation. The resulting expression for E in units of kg/cm^2 is given as

$$E \ (\text{kg}/\text{cm}^2) = \frac{56 + 7.66H_A}{2.67r(254 - 2.54H_A)}, \quad (2.1.2)$$

where H_A is the Shore A hardness. To express the modulus in MPa units, the equation must be multiplied by $1 \text{ kg/cm}^2 \approx 0.0981 \text{ MPa}$. Substituting $r = 0.0515$ as reported in referred citation, it gives

$$E \text{ (MPa)} = \frac{0.0981 (56 + 7.66 H_A)}{0.137505 (254 - 2.54 H_A)}. \quad (2.1.3)$$

This expression is derived from Gent's analytical approximation, which assumes small indentation depths and linear, isotropic, elastic material behavior. The constants in the equation originate from the mechanics and geometry of the Shore A durometer, including the calibrated spring force, the indenter displacement range, and the conical tip geometry approximated as a flat punch. Gent's model offers a continuous mapping across the Shore A scale and remains a convenient approximation for estimating the elastic modulus without requiring nonlinear simulations or experimental calibration.

According to [6] and [7] ideally, the hardness scale should convert a modulus range of $0 \rightarrow \infty$ to a hardness scale of 0–100. Clearly Eq. 2.1.3 fulfills this for $H_A = 100$ but not for $H_A = 0$, and there are small departures from the master curve at H_A values below 40 given in Gent's paper. The approximation is illustrated in Figure 2.1.7.

2.1.4.2 Finite Strain Modeling by Qi et al.

Qi et al. [5] established a relationship between Shore A hardness and elastic modulus by performing fully nonlinear finite element simulations of the durometer indentation process. As for the elastomer's material model Neo-Hookean were used, and the Shore A test was replicated with axisymmetric geometry and appropriate boundary conditions. The reaction force during indentation was computed, and the resulting force–displacement curves were intersected with the calibrated spring line of the Shore A durometer to extract corresponding hardness values. (In my thesis I use a similar approach.) From the simulation results, the authors derived an empirical logarithmic fit to describe the relationship between the elastic modulus E (in MPa) and Shore A hardness H_A

$$\log_{10} E = 0.0253 H_A - 0.6403, \quad \text{for } 20 < H_A < 80. \quad (2.1.4)$$

Unlike Gent's formula, which is based on classical elasticity and is supported by physical measurements, Qi's model is a purely simulation-driven, empirical fit. As such, its accuracy and applicability are limited to the simulation setup and material model used. It assumes Neo-Hookean behavior, which may not be representative for all elastomers.

2.1.4.3 Summary

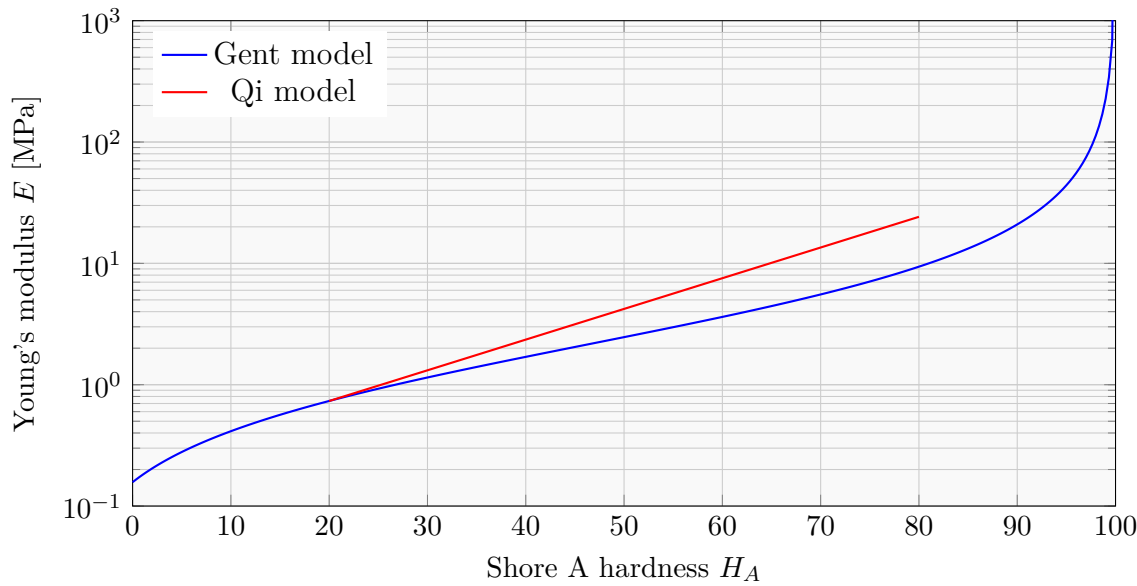


Figure 2.1.7: Comparison of the Gent and Qi models relating H_A to E .

2.2 Theory of Hyperelasticity

The mechanical response of common material under loading is characterized by an initial linear part, followed by yielding and plastic deformation. As Figure 2.2.1, shows metals initially obey Hooke's law, where σ is linearly proportional to ε . Upon exceeding the elastic limit, metals experience irreversible plastic deformation, meaning that upon unloading, the material does not return to its original form.

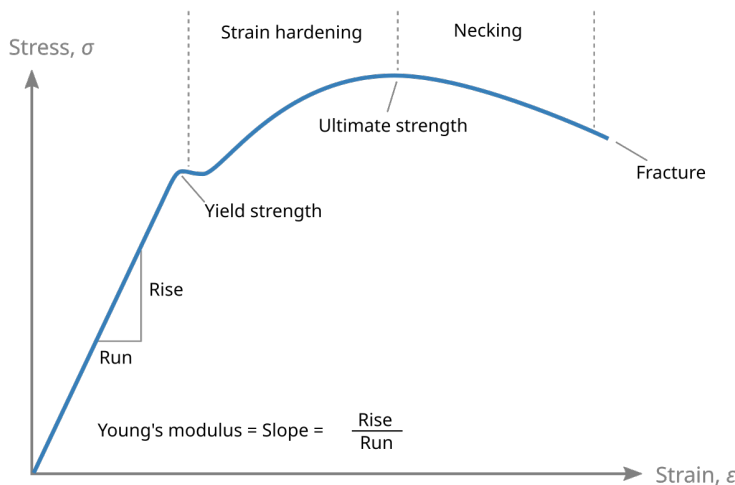


Figure 2.2.1: Stress-strain curve for a typical ductile material. (Source: commons.wikimedia.org)

In contrast, hyperelastic materials, such as elastomers, follows a different behavior. Their $\sigma - \varepsilon$ relation is highly nonlinear as Figure 2.2.2 shows. These materials are capable to undergo extremely large deformations, even exceeding several hundred percent strain and yet capable to fully recover their original form upon unloading.

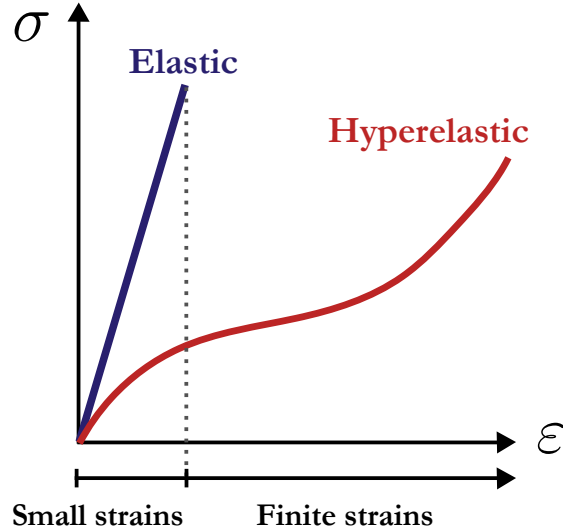


Figure 2.2.2: $\sigma - \varepsilon$ curve for a typical hyperelastic material with large deformation.

Rubberlike (elastomer) materials are typically modeled as nearly incompressible, therefore $\nu \approx 0.5$. Their behavior deviates from Hooke's law. Instead of a linear $\sigma - \varepsilon$ relation, hyperelastic behavior is described with strain energy density functions(W), that expresses the stored energy per unit volume as a function of the deformation state. Material models like Neo-Hookean, Mooney-Rivlin, and Ogden can capture the response of these materials across a wider strain regime.

2.2.1 Strain Energy Potentials

The behaviour of hyperelastic materials can be captured using strain energy function W , which tells us how much elastic energy is stored when the material is deformed. To describe this deformation, we use the right Cauchy-Green deformation tensor

$$\mathbf{C} = \mathbf{F}^T \mathbf{F}, \quad (2.2.1)$$

where \mathbf{F} is the deformation gradient. \mathbf{C} is a symmetric tensor that isolates material deformation (stretching and shortening) from rigid body rotations. The strain energy density function W is expressed with the help of principal stretches ($\lambda_1, \lambda_2, \lambda_3$), which are the square roots of the eigenvalues of \mathbf{C} , or the scalar invariants (I_1, I_2, I_3) of \mathbf{C} .

These invariants can be calculated as

$$I_1 = \text{tr}(\mathbf{C}) = \lambda_1^2 + \lambda_2^2 + \lambda_3^2, \quad (2.2.2)$$

$$I_2 = \frac{1}{2} [(\text{tr } \mathbf{C})^2 - \text{tr}(\mathbf{C}^2)] = \lambda_1^2 \lambda_2^2 + \lambda_2^2 \lambda_3^2 + \lambda_3^2 \lambda_1^2, \quad (2.2.3)$$

$$I_3 = \det(\mathbf{C}) = J^2. \quad (2.2.4)$$

For incompressible materials, where the volume ratio $J = \det \mathbf{F} = 1$, the third invariant I_3 becomes constant and can be excluded from the formulation. In cases like this, the strain energy simplifies to a function of I_1 and I_2 :

$$W = W(I_1, I_2). \quad (2.2.5)$$

The choice of the specific form of W leads to different hyperelastic models. Simple models like the Neo-Hookean are based primarily on I_1 , while more complex models like Mooney-Rivlin and Ogden consider both I_1 , I_2 , and principal stretches. Throughout this section, the materials are assumed to be nearly incompressible, with Poisson's ratio $\nu \approx 0.5$ and elastic volume ratio $J \approx 1$. This assumption simplifies the strain energy functions used in all models presented below.

2.2.2 Neo-Hookean Model

The Neo-Hookean model is one of the simplest and most widely used hyperelastic models, mostly for moderate deformations. Based on [8] in Abaqus, the Neo-Hookean strain energy potential is defined as

$$W = C_{10}(I_1 - 3) + \frac{1}{D_1}(J - 1)^2 \quad (2.2.6)$$

where C_{10} and D_1 are material parameters, I_1 is the first invariant of the deviatoric part of the deformation, and J is the elastic volume ratio. The initial shear modulus μ_0 and bulk modulus K_0 are related to the material parameters as:

$$\mu_0 = 2C_{10}, \quad K_0 = \frac{2}{D_1}, \quad (2.2.7)$$

$$E = 3\mu_0 = 6C_{10}. \quad (2.2.8)$$

Thus, increasing the C_{10} parameter directly increases the shear modulus μ_0 , and consequently, the Young's modulus E . A higher C_{10} value leads to a stiffer material response under deformation.

2.2.3 Ogden Model

The Ogden model provides a highly flexible framework to describe the nonlinear elastic behavior of hyperelastic materials over a wide range of deformations. It generalizes the

strain energy potential by considering the principal stretches raised to different powers. The form of the Ogden strain energy potential is given by:

$$W = \sum_{i=1}^N \frac{2\mu_i}{\alpha_i^2} (\lambda_1^{\alpha_i} + \lambda_2^{\alpha_i} + \lambda_3^{\alpha_i} - 3) + \sum_{i=1}^N \frac{1}{D_i} (J - 1)^{2i}, \quad (2.2.9)$$

where λ_i are the principal stretches, N is the number of terms in the expansion, and μ_i , α_i , and D_i are material parameters. The initial shear modulus μ_0 and bulk modulus K_0 for the Ogden model are given by

$$\mu_0 = \sum_{i=1}^N \mu_i, \quad K_0 = \frac{2}{D_1}. \quad (2.2.10)$$

Depending on the number of terms N , the Ogden model can fit a wide range of material behaviors.

Influence of Parameters:

- The parameters μ_i primarily control the base stiffness of the material. Increasing μ_i results in a higher overall stress response.
- The parameters α_i govern the degree of nonlinearity and strain stiffening behavior. Larger α_i values result in more pronounced strain stiffening at higher deformations showed in Figure 4.2.2.

2.2.3.1 Ogden Model with N=1

For $N = 1$, the strain energy potential simplifies to

$$W = \frac{2\mu_1}{\alpha_1^2} (\lambda_1^{\alpha_1} + \lambda_2^{\alpha_1} + \lambda_3^{\alpha_1} - 3) + \frac{1}{D_1} (J - 1)^2. \quad (2.2.11)$$

This single-term Ogden model can capture moderate nonlinearity and is often sufficient for simple elastomeric materials where the strain range is not extremely large while the elastic modulus is calculated as

$$E = 3\mu_1. \quad (2.2.12)$$

2.2.3.2 Ogden Model with N=2

For $N = 2$, the strain energy potential becomes:

$$W = \sum_{i=1}^2 \frac{2\mu_i}{\alpha_i^2} (\lambda_1^{\alpha_i} + \lambda_2^{\alpha_i} + \lambda_3^{\alpha_i} - 3) + \sum_{i=1}^2 \frac{1}{D_i} (J - 1)^{2i} \quad (2.2.13)$$

Using two terms (μ_1, α_1 and μ_2, α_2) gives the model more flexibility to handle strongly nonlinear behavior across a wider range of deformations. This is especially helpful when

dealing with complex elastomers or soft biological tissues, where a single-term model often isn't enough to match the actual stress-strain response. With this formulation the elastic modulus is determined as

$$E = 3(\mu_1 + \mu_2). \quad (2.2.14)$$

2.2.4 Mooney-Rivlin Model

The Mooney-Rivlin model builds on the Neo-Hookean approach by also taking into account the second invariant of the deviatoric deformation tensor. This makes it better suited for describing material behaviour over a wider range of moderate deformations. The strain energy function for the Mooney-Rivlin model is written as

$$W = C_{10}(I_1 - 3) + C_{01}(I_2 - 3) + \frac{1}{D_1}(J - 1)^2, \quad (2.2.15)$$

where

- C_{10} and C_{01} are material constants related to the material's response to deformation,
- D_1 is a parameter associated with compressibility.

The initial shear modulus μ_0 and the bulk modulus K_0 are related to the material parameters as

$$\mu_0 = 2(C_{10} + C_{01}), \quad K_0 = \frac{2}{D_1}. \quad (2.2.16)$$

Assuming incompressibility ($\nu \approx 0.5$), the elastic modulus E can be estimated as

$$E = 3\mu_0 = 6(C_{10} + C_{01}). \quad (2.2.17)$$

2.2.5 Derivation of the Uniaxial Stress Expression

The Neo-Hookean strain energy density function is defined as

$$W = C_{10}(I_1 - 3) + \frac{1}{D_1}(J - 1)^2. \quad (2.2.18)$$

where C_{10} and D_1 are material parameters, I_1 is the first invariant of the isochoric right Cauchy-Green deformation tensor, and J is the elastic volume ratio. Assuming nearly incompressible materials it simplifies the strain energy function to

$$W = C_{10}(I_1 - 3). \quad (2.2.19)$$

Under uniaxial loading, the principal stretches satisfy the relation of

$$\lambda_2 = \lambda_3 = \lambda_1^{-1/2}, \quad (2.2.20)$$

due to the incompressibility constraint $\lambda_1\lambda_2\lambda_3 = 1$. Thus, the first invariant I_1 can be expressed as

$$I_1 = \lambda_1^2 + 2\lambda_1^{-1}. \quad (2.2.21)$$

Substituting this into the strain energy function, it gives

$$W = C_{10}(\lambda_1^2 + 2\lambda_1^{-1} - 3). \quad (2.2.22)$$

The nominal stress P_1 is obtained by differentiating W with respect to λ_1

$$P_1 = \frac{\partial W}{\partial \lambda_1} = C_{10} \left(2\lambda_1 - 2\lambda_1^{-2} \right), \quad (2.2.23)$$

which simplifies to

$$P_1^{NH} = 2C_{10} \left(\lambda_1 - \lambda_1^{-2} \right). \quad (2.2.24)$$

Thus, the uniaxial stress expression for the Neo-Hookean material is obtained as shown in Table 2.2.1. The uniaxial stress expression can be determined the same way for the other models too.

Table 2.2.1: Uniaxial stress solutions for different hyperelastic models

Model	Uniaxial Stress Expression (incompressible)	
Neo-Hookean	$P_1^{NH} = 2C_{10} \left(\lambda_1 - \lambda_1^{-2} \right)$	(2.2.25)
1st-order Ogden	$P_1^{O1} = 2\frac{\mu_1}{\alpha_1} \left(\lambda_1^{\alpha_1-1} - \lambda_1^{-\alpha_1/2-1} \right)$	(2.2.26)
2nd-order Ogden	$P_1^{O2} = 2\frac{\mu_1}{\alpha_1} \left(\lambda_1^{\alpha_1-1} - \lambda_1^{-\alpha_1/2-1} \right) + 2\frac{\mu_2}{\alpha_2} \left(\lambda_1^{\alpha_2-1} - \lambda_1^{-\alpha_2/2-1} \right)$	(2.2.27)
Mooney-Rivlin	$P_1^{MR} = 2C_{10} \left(\lambda_1 - \lambda_1^{-2} \right) + 2C_{01} \left(1 - \lambda_1^{-3} \right)$	(2.2.28)

Even though the strain energy density function W gives a consistent way to describe how the material behaves, it's the nominal stress P_1 that really matters when it comes to practical use and comparing with experimental results. The stress response P_1 must be derived from W because mechanical equilibrium equations, finite element analyses, and material model fitting procedures are all based on forces and stresses, not internal energy alone. Therefore, the transformation from W to P_1 is needed for connecting theoretical material models to measurable quantities such as stress-stretch curves.

3

Measurements

3.1 Uniaxial Compression Tests

Elastomers are nonlinear, nearly incompressible materials, making their mechanical behavior complex. For this reason, obtaining accurate material characteristics, such as the stretch–stress (λ - P) response is crucial for both theoretical modeling and simulation. Uniaxial compression is particularly well-suited for this task. Due to the material’s incompressibility, the product of the principal stretch ratios must remain constant during deformation as

$$J = \det \mathbf{F} = \lambda_1 \lambda_2 \lambda_3 = 1. \quad (3.1.1)$$

In a uniaxial compression test, the specimen is compressed along one axis ($\lambda_1 < 1$), and expands symmetrically in the transverse directions ($\lambda_2 = \lambda_3 = \lambda_1^{-1/2} > 1$) to preserve volume. This induces a multiaxial deformation state, even though only a single axis is externally loaded. As a result, the material response observed in uniaxial compression inherently reflects characteristics similar to those seen in biaxial loading. This makes uniaxial tests not only easy to do but especially informative for capturing the nonlinear behavior of incompressible materials. Furthermore, compression tests are experimentally stable and allow large deformations without failure, unlike tension tests which are prone to necking or rupture. Thus, uniaxial compression provides a reliable, efficient, and physically rich means of identifying the constitutive behavior of soft materials like elastomers. Therefore in order to evaluate the nonlinear stress-stretch characteristics of the investigated materials, uniaxial compression tests were performed. The geometry of the specimens used in the compression tests was based on the recommendation of ISO 3386 standard, which suggests

that specimens should be right parallelepipeds with a minimum width-to-thickness ratio of 2:1. Therefore, five 25 mm × 25 mm specimens were stacked together to achieve the minimum thickness requirement, as shown in Figure 3.1.1.

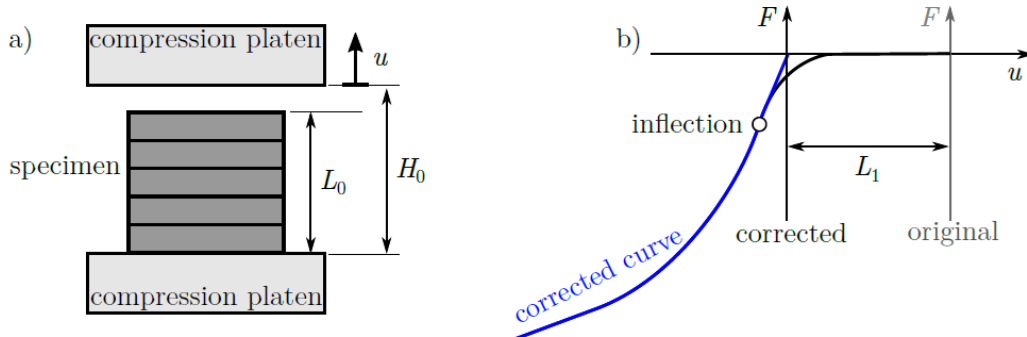


Figure 3.1.1: a) The layout of the compression test with stacked specimens and b) the concept of slack correction method.

The measurements were conducted at the Laboratory of the Department of Applied Mechanics, BME, using an Instron 3345 Single Column Universal Testing System, equipped with an Instron model 2519-107 5kN load cell. The compression test was performed with a cross-head speed of $v = 10 \text{ mm/min}$ to minimize viscoelastic effects. The initial platen separation was $H_0 = 26 \text{ mm}$ and the maximal displacement was $u_{\max} = 15 \text{ mm}$. During the measurements, at each sampling point, the corresponding load F and displacement u values were recorded. The initial separation of the platens H_0 was greater than the initial specimen height L_0 , resulting in zero load at the beginning as the platens did not initially contact the specimen. The actual starting point was corrected using the slack correction method illustrated in Figure 3.1.1b.

An inflection point can be observed in the initial region of the measured $F-u$ curve. This inflection was corrected with a so called *slack correction*, which is done by extrapolating the tangent line from the inflection point to determine the corrected displacement L_1 , allowing the calculation of the actual specimen height as

$$L_0 = H_0 - L_1. \quad (3.1.2)$$

From the corrected $F-u$ data, the engineering stress P_1 and longitudinal stretch λ_1 were calculated using:

$$\lambda_1 = 1 + \frac{u}{L_1}, \quad P_1 = \frac{F}{A_0}, \quad (3.1.3)$$

where the initial cross-sectional area $A_0 = 625 \text{ mm}^2$. The applied specimens and the process of the compression test are shown in Figure 3.1.2. The results of the compression tests, depicting the engineering stress-stretch behavior for Elastosil, Rubber, and Silicone, are presented in Figure 3.2.2.

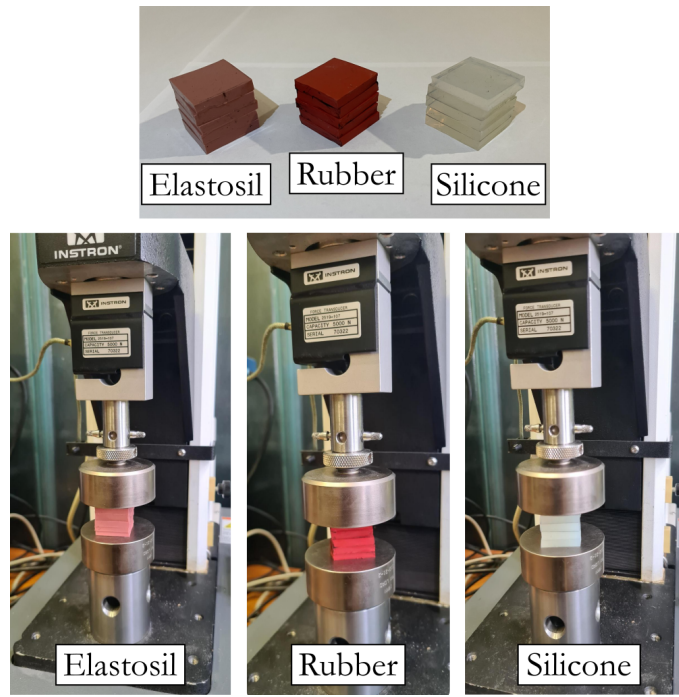


Figure 3.1.2: Specimens and the layout of compression test.

3.2 Uniaxial Compression Results

To quantitatively evaluate and compare the performance of various hyperelastic material models, nonlinear curve fitting was performed on the averaged uniaxial compression data for each tested material. The four fitted models can be seen in Section 3.3.

Before fitting, the raw measurement data was exported as CSV files containing force and displacement values then processed using a custom Python script. The workflow included slack correction, truncation after peak force, unit conversions, and averaging multiple measurements to obtain a single representative stress–stretch curve, as illustrated in Figure 3.2.1. Figure 3.2.2 shows the final processed stress–stretch curves ($P - \lambda$) for the three materials.

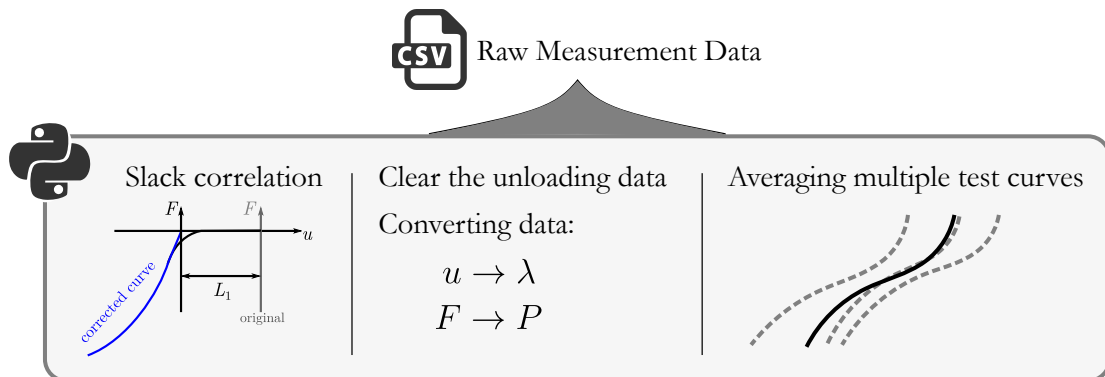


Figure 3.2.1: Data processing workflow applied to raw measurement data.

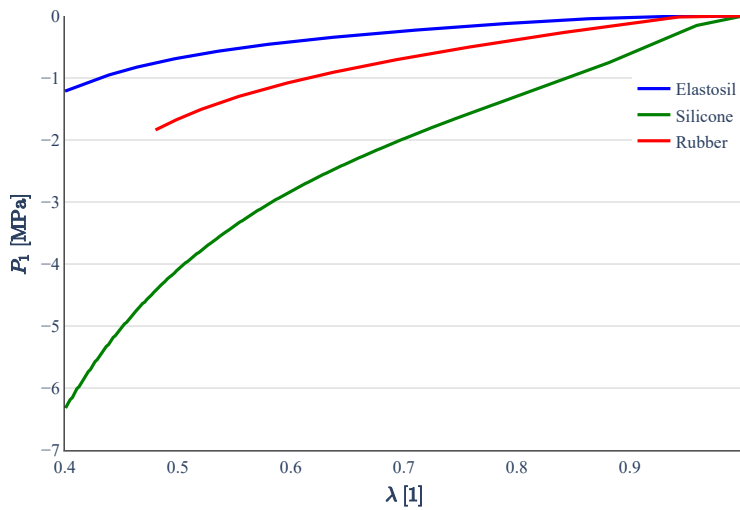


Figure 3.2.2: Result of uniaxial compression test: averaged stress–stretch curves.

After preprocessing, the averaged curves were fit to each constitutive model, resulting in a set of optimized material parameters for each case. The accuracy of the fits was assessed using the coefficient of determination (R^2), while the corresponding elastic modulus (E) was calculated based on the model-specific analytical expressions summarized in Table 2.2.1.

3.3 Material Model Fitting

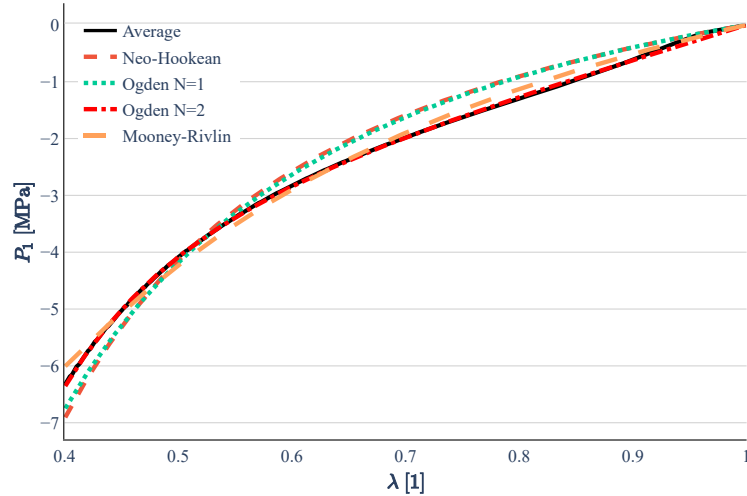
The following subsections present the fitting results for each material, including a figure of the fitted model curves and a summary table of the results.

3.3.1 Silicone

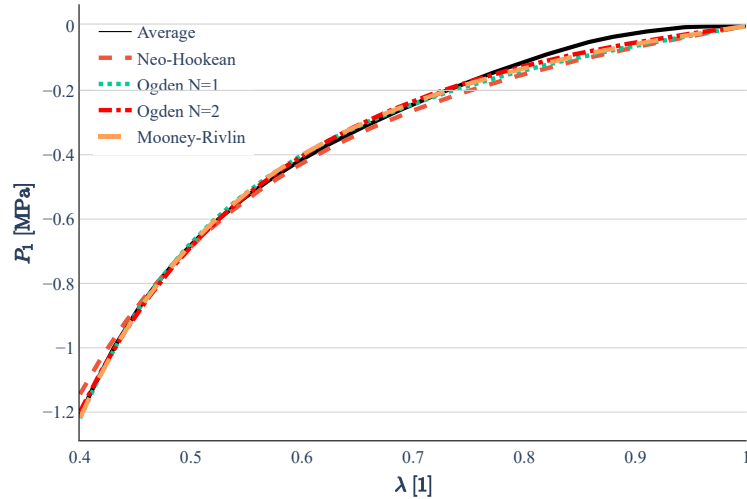
For the Silicone material, all models performed reasonably well, but the Mooney-Rivlin and Ogden $N = 2$ models achieved superior accuracy with R^2 values exceeding 99%. The fitted parameters provide a reliable basis for simulation input in Abaqus.

Table 3.3.1: Fitted hyperelastic parameters for **Silicone**.

Model	Fitted parameters	R^2 [%]	E [MPa]
Neo-Hookean	$C_{10} = 0.592$ MPa	96.74	5.797
Mooney-Rivlin	$C_{10} = 0.966$ MPa, $C_{01} = -0.181$ MPa	99.51	4.712
Ogden $N = 1$	$\mu_1 = 1.160$ MPa, $\alpha_1 = 1.193$	97.31	3.480
Ogden $N = 2$	$\mu_1 = 4.343$ MPa, $\alpha_1 = 2.324$ $\mu_2 = -2.286$ MPa, $\alpha_2 = -0.768$	99.97	6.171

Figure 3.3.1: Model fitting results for **Silicone**.

3.3.2 Elastosil

Figure 3.3.2: Model fitting results for **Elastosil**.Table 3.3.2: Fitted hyperelastic parameters for **Elastosil**.

Model	Fitted parameters	R^2 [%]	E [MPa]
Neo-Hookean	$C_{10} = 0.098$ MPa	99.22	0.406
Mooney-Rivlin	$C_{10} = 0.068$ MPa, $C_{01} = 0.015$ MPa	99.69	0.493
Ogden $N = 1$	$\mu_1 = 0.186$ MPa, $\alpha_1 = 3.065$	99.59	0.560
Ogden $N = 2$	$\mu_1 = 0.103$ MPa, $\alpha_1 = -0.714$ $\mu_2 = 0.039$ MPa, $\alpha_2 = -0.714$	99.78	0.427

Elastosil exhibited highly consistent results across all four models, with R^2 values near or above 99%. The moderate stiffness reflected in the elastic modulus is aligned with expected values, validating the material behavior for finite element analysis.

3.3.3 Rubber

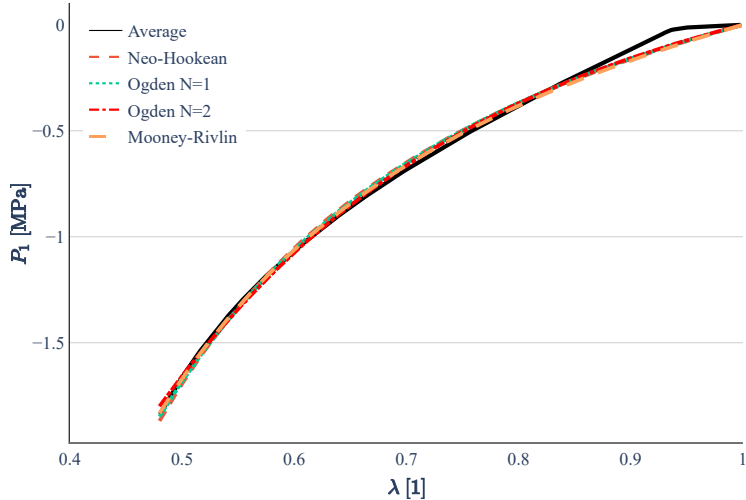


Figure 3.3.3: Model fitting results for **Rubber**.

Table 3.3.3: Fitted hyperelastic parameters for **Rubber**.

Model	Fitted parameters	R^2 [%]	E [MPa]
Neo-Hookean	$C_{10} = 0.242$ MPa	99.63	1.615
Mooney-Rivlin	$C_{10} = 0.269$ MPa, $C_{01} = -0.015$ MPa	99.68	1.522
Ogden $N = 1$	$\mu_1 = 0.465$ MPa, $\alpha_1 = 1.139$	99.69	1.396
Ogden $N = 2$	$\mu_1 = 12.906$ MPa, $\alpha_1 = -0.906$ $\mu_2 = -12.457$ MPa, $\alpha_2 = -0.944$	99.75	1.346

The Rubber material showed significant variation in R^2 values across models, with the Neo-Hookean fit notably underperforming. More flexible models like Mooney-Rivlin and Ogden $N = 2$ achieved high accuracy. The calculated modulus values are consistent with the expected mechanical range and provide trustworthy data for Abaqus implementation.

4

FE model development

This chapter defines the base finite element (FE) model and key setup steps, enabling later sections to focus solely on task-specific modifications.

4.1 Model Objectives and Approach

The objective of the FE model is to replicate the standardized Shore hardness test through simulation, extracting hardness from the material's indentation response. By modeling the interaction between a rigid indenter and an elastomeric specimen, Shore hardness is derived from the resulting force–displacement behavior. This enables flexible, repeatable analysis of materials under controlled conditions and supports the study of geometric and constitutive effects. The model uses an axisymmetric setup based on ASTM D2240, with parametrized geometry, material definitions, and boundary conditions. The setup was designed for easy automation, allowing consistent model generation and efficient evaluation of multiple configurations. It supports a parametric study in which material models (e.g., Neo-Hookean, Ogden) and specimen dimensions are varied to assess the influence of nonlinear behavior and geometry on Shore hardness.

4.2 Shore Hardness Calculation from FE Simulation

Shore hardness is calculated from the simulated force–indentation curve using ABAQUS by identifying the force corresponding to a standardized indentation depth, as specified in

ASTM D2240. This value is then used to determine hardness using the standard conversion method.

Model Setup

The geometry of the test specimen is created as a 2D axisymmetric part, with dimensions defined to ensure that boundary effects are minimized, in accordance with ASTM recommendations. The indenter is modeled as an axisymmetric rigid analytic surface with geometry matching the Shore-A configuration. The mesh for the elastomeric domain uses structured quadrilateral elements (CAX4RH) with local refinement near the contact region to capture high gradients in stress and strain. A hybrid element formulation is used to handle the incompressibility of hyperelastic materials. The indenter is meshed with an analytical surface and a reference point is used for applying boundary conditions and extracting reaction forces.

The contact interaction between the indenter and the specimen is defined using a surface-to-surface finite sliding formulation. A small penalty friction coefficient is used to improve numerical stability and realism.

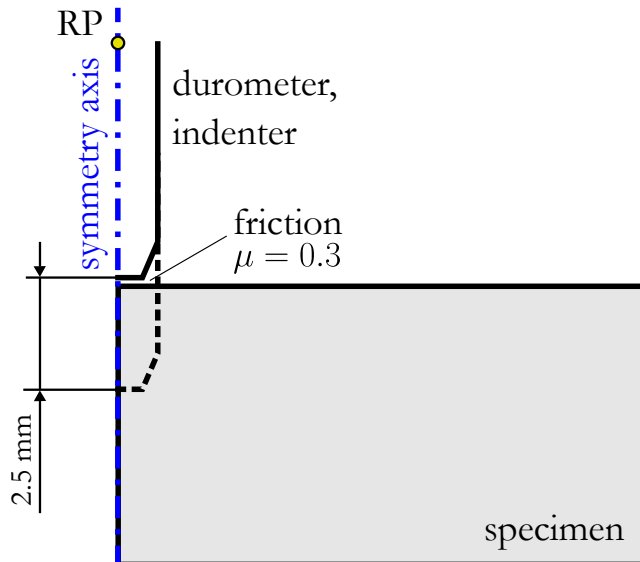


Figure 4.2.1: FE model setup with rigid indenter and elastomer specimen.

Simulation Procedure

Each simulation step involves vertically displacing the indenter into the elastomeric specimen. Boundary conditions include full constraint at the base and symmetry along the central axis. The indenter is displaced using a prescribed vertical displacement of 2.5 mm (+ 0.1 mm initial gap), which corresponds to the maximum possible penetration allowed in Shore hardness testing.

During the simulation, the reaction force acting on the indenter is recorded as it presses into the specimen. In the post-processing phase, the Shore hardness value is determined by identifying the point where the reaction force from the material balances the force from the calibrated spring of the durometer. This means that if such a force equilibrium occurred during an actual test, the indenter would have sunk to exactly this depth, and the corresponding spring reading would define the Shore hardness.

Material Models

This study evaluates three hyperelastic material models to capture the nonlinear response of elastomeric specimens:

- **Neo-Hookean model**, defined by C_{10} and D_1 ;
- **Ogden model with one term ($N=1$)**, defined by μ_1 , α_1 , and D_1 ;
- **Ogden model with two terms ($N=2$)**, defined by μ_i , α_i , and D_i for $i = 1, 2$.

Material parameters were applied using Abaqus' built-in `Hyperelastic` function with the `volumetricResponse=VOLUMETRIC_DATA` flag to model nearly incompressible behavior by setting $D_i = 0$.

Note

For specific choices of its parameters, the Ogden model can reproduce both the Neo-Hookean and Mooney–Rivlin models:

- The **Neo-Hookean model** is recovered from the Ogden model when $N = 1$, $\alpha_1 = 2$, and $\mu_1 = C_{10}$. Substituting into the Ogden form gives us the same strain energy expression as the Neo-Hookean model.
- The **Mooney–Rivlin model** is produced by setting $N = 2$, $\alpha_1 = 2$, $\alpha_2 = -2$, and choosing μ_1 and μ_2 such that

$$C_{10} = \frac{\mu_1}{\alpha_1^2}, \quad C_{01} = \frac{\mu_2}{\alpha_2^2}.$$

Figure 4.2.2 illustrates the model's sensitivity: α_1 governs nonlinearity and strain stiffening, while μ_1 scales the stress response. The initial material model parameter values used in the simulations are listed in Tables 3.3.1–3.3.3 in the Measurements section.

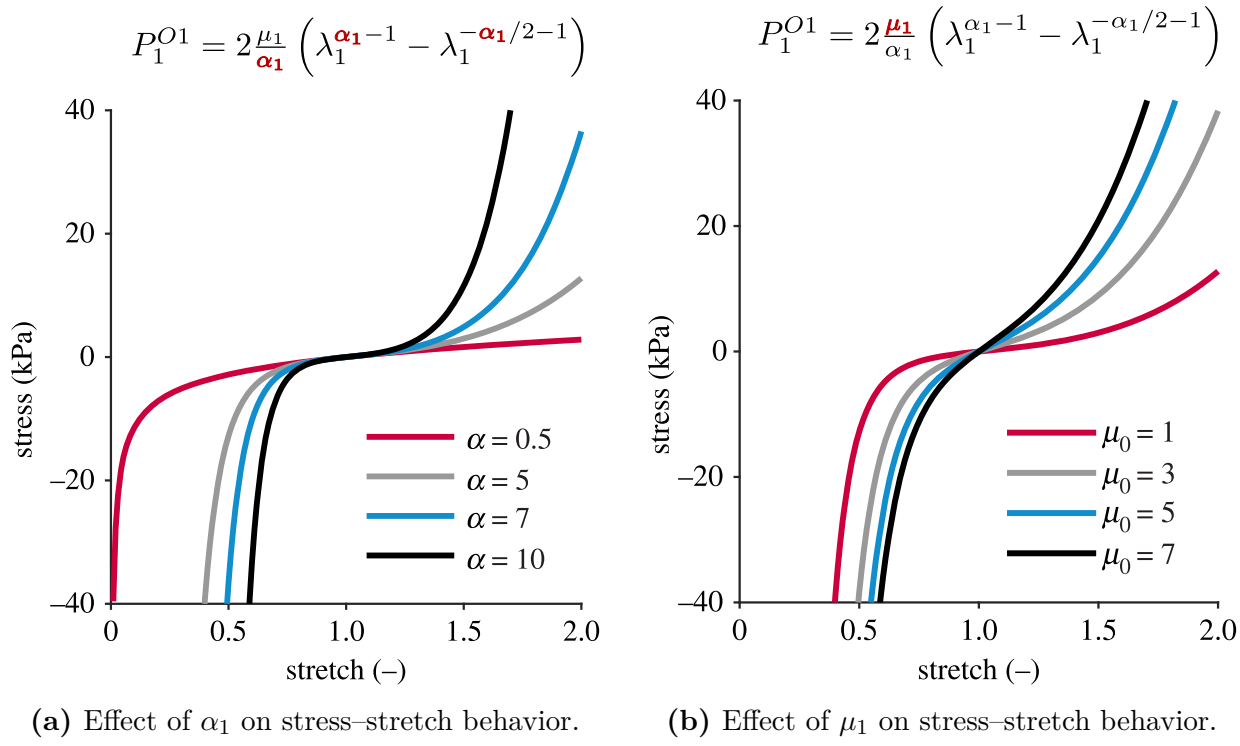


Figure 4.2.2: Ogden model response to pure shear. (a) Sensitivity to the nonlinearity parameter α_1 with $\mu_1 = 1$. (b) Sensitivity to μ_1 with $\alpha_1 = 5$. [9]

Post-Processing and Hardness Extraction

The Shore A hardness value was obtained from the finite element simulation by comparing the reaction force of the indenter with the known spring response of the Shore A durometer. The standard force-depth relationship of the durometer is defined by [10] as

$$F_s = 0.55 + k_A \Delta L, \quad (4.2.1)$$

where $k_A = 3000$ N/m and $\Delta L = L_1 - L_0$ is the indentation depth, as illustrated in Figure 2.1.2. Using the linear calibration relation $\Delta L = 0.025(100 - H_A)$, the force can be written directly as a function of hardness:

$$F_s = 0.55 + 0.075 H_A. \quad (4.2.2)$$

The method implemented in this study determines the Shore A hardness value by finding the intersection point between the force-indentation response obtained from the simulation and the calibrated durometer spring force line. This approach is visualized in Figure 4.2.3.

However, direct use of the raw simulation output is not sufficient. Preprocessing is required to convert the displacement and force data into the form compatible with the calibrated equation. The following transformations are applied.

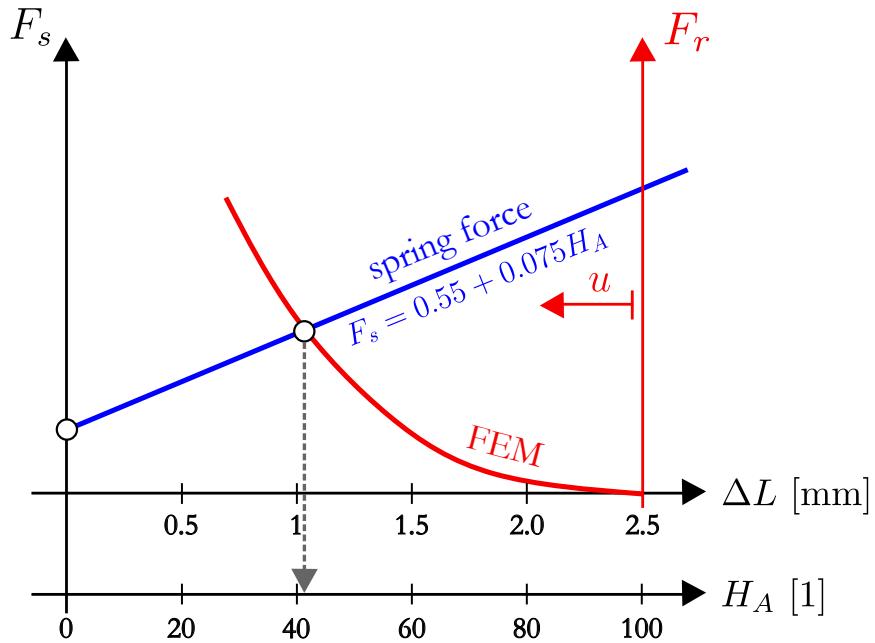


Figure 4.2.3: Schematic of the method to determine the Shore A hardness value from the FE-simulation result ($F - u$ curve) and the durometer spring characteristics.

Transformation Steps

1. Discard values where $|U_2| \leq 0.1$ mm.
2. Compute indentation depth: $U_{\text{rev}} = 2.5 - (|U_2| - 0.1)$
3. Map indentation to Shore hardness: $H_A = \frac{U_{\text{rev}}}{0.025}$
4. Flip reaction force: $F_{\text{rev}} = |RF_2|$

```

1  delta_L_limit = 0.1
2  with open("Force_Displacement.csv") as file:
3      reader = csv.reader(file, delimiter=';')
4      next(reader)
5
6      for row in reader:
7          u2 = float(row[1])
8          rf2 = float(row[2])
9          if abs(u2) > delta_L_limit:
10              u_rev = 2.5 - (abs(u2) - delta_L_limit)
11              ha = u_rev / 0.025
12              f_rev = abs(rf2)
13              displacements.append(u_rev)
14              reaction_forces.append(f_rev)

```

Listing 4.1: Python logic for transforming FE output.

Once the simulation data were preprocessed and transformed into Shore A hardness domain, the resulting discrete dataset $\{(H_{A,i}, F_i)\}_{i=1}^n$ was treated as a sampled representation of a continuous force function. To facilitate numerical comparison with the durometer's

spring response, the data were linearly interpolated using a one-dimensional function as

$$F_{\text{FEM}}(H_A) := \mathcal{I}(\{(H_{A,i}, F_i)\}_{i=1}^n), \quad (3.2.11)$$

where $\mathcal{I}(\cdot)$ denotes the interpolation operator, resulting in a continuous function that approximates the FEM force response as a function of Shore-A hardness. The reference force–hardness relationship defined by the calibrated Shore-A durometer is given analytically by

$$F_s(H_A) = 0.55 + 0.075 \cdot H_A, \quad (3.2.12)$$

where $H_A \in [0, 100]$. The Shore A hardness corresponding to the simulation result is determined by solving the nonlinear equation

$$F_{\text{FEM}}(H_A) - F_s(H_A) = 0, \quad (3.2.13)$$

or equivalently, finding the root of the function

$$f(H_A) := F_{\text{FEM}}(H_A) - (0.55 + 0.075 \cdot H_A). \quad (3.2.14)$$

The solution $H_A^* \in [0, 100]$ is computed using a numerical root-finding method satisfying

$$f(H_A^*) = 0. \quad (3.2.15)$$

The resulting value H_A^* represents the Shore A hardness corresponding to the intersection of the simulated force response and the calibrated durometer spring line.

Need for Multiple Material Models and Geometry Variations

To accurately simulate Shore hardness testing of elastomeric materials, it is essential to account for the wide range of mechanical behaviors that different materials can exhibit. In this study, two hyperelastic material models are considered: the Neo-Hookean model and the Ogden model with one term ($N = 1$).

The Neo-Hookean model offers a simple yet effective representation of rubber-like materials for moderate deformations. It assumes Gaussian chain statistics and is primarily characterized by a single material constant, making it computationally efficient and suitable for baseline studies. However, it tends to underpredict stress at large strains, which can limit its applicability for materials experiencing significant nonlinear deformation under indentation. To address this, the Ogden model ($N=1$) is also employed. It captures nonlinear stress–strain behavior more accurately by introducing an additional shape parameter

(α), allowing better modeling of stiffening effects at large strains. This model is particularly useful when the elastomer exhibits pronounced strain-hardening during indentation, as seen in many commercial rubber compounds and soft biological tissues.

In addition to material variations, different specimen geometries are simulated. Varying the thickness and dimensions of the test sample helps evaluate the influence of boundary effects and ensures compliance with ASTM standards for indentation testing. Geometry variation is also necessary to study how scale influences the force–displacement response and the resulting Shore hardness reading.

4.3 Geometry and Indenter Setup

The finite element model uses an axisymmetric representation of the Shore hardness test setup, which allows efficient computation while accurately capturing the key mechanical behavior of the system. The test specimen is modeled as a cylindrical elastomer block subjected to indentation by a rigid indenter.

Specimen Geometry

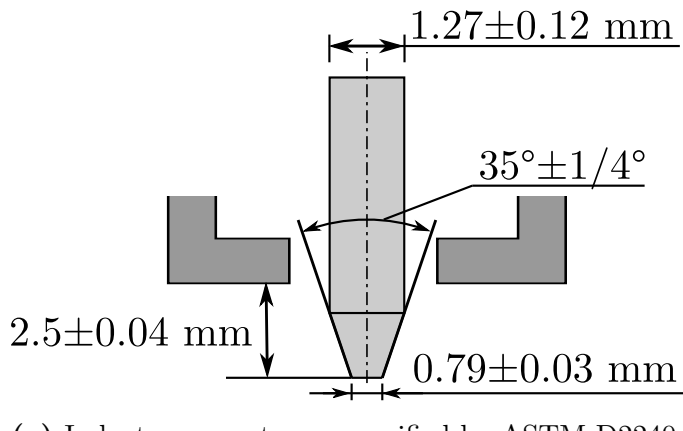
The test specimen is a cylindrical puck in 3D, which becomes a rectangle when represented as 2D axisymmetric model. This simplification retains the essential deformation behavior while reducing computational cost. The cross-section is defined by the specimen's radius and height, chosen to minimize boundary effects. The radius is set to be at least five times the indenter diameter, and the height is sufficient to prevent the bottom support from influencing local deformation near the indenter. These dimensions align with ASTM D2240 recommendations and ensure the validity of the simulated indentation response.

Indenter Geometry and Assumptions

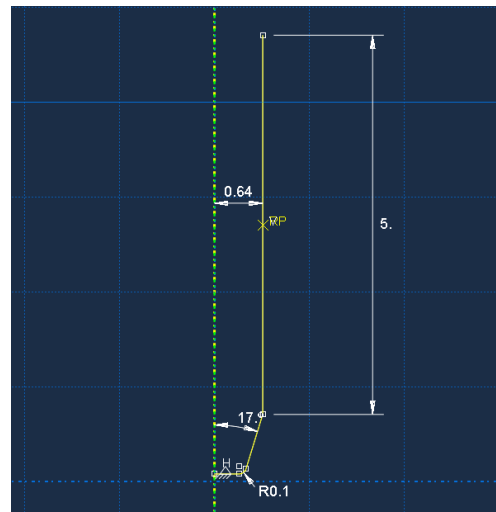
The indenter geometry follows ASTM D2240 specifications for Shore A hardness testing. It is modelled as a rigid body, which simplifies the simulation and reflects the relatively high stiffness of real-world indenters compared to the tested elastomeric materials. The key dimensions of the indenter are:

- Diameter of the cylindrical shaft: 1.27 ± 0.12 mm
- Cone angle: $35^\circ \pm 1/4^\circ$
- Tip diameter: 0.79 ± 0.03 mm
- Total length of protrusion: 2.5 ± 0.04 mm

These dimensions are illustrated in Figure 4.3.1, which shows both the nominal geometry and its implementation in the FE model.



(a) Indenter geometry as specified by ASTM D2240.



(b) Indenter sketch as implemented in Abaqus.

Figure 4.3.1: Cross-sectional view of the Shore A indenter geometry. (a) Standard dimensions. (b) FE model input geometry with tip rounding.

To ensure numerical stability in the simulation, a small rounding with a radius of 0.1 mm was applied at the tip of the cone. This modification has negligible effect on the overall force–displacement response but was essential for convergence.

4.4 Boundary Conditions and Loading

Axisymmetry was assumed in the finite element model to reduce computational effort while preserving geometric and loading fidelity. The specimen was modeled in 2D, with boundary conditions reflecting symmetry, physical constraints, and loading conditions representative of the Shore A hardness test.

Symmetry Conditions

The axis of symmetry lies along the left vertical edge of the specimen. A symmetry boundary condition is applied by constraining horizontal displacement ($U_1 = 0$), while vertical displacement (U_2) and in-plane rotation (UR_3) remain unconstrained.

Specimen Constraints

The bottom edge of the specimen is fully constrained with an *encastre* boundary condition that fixes all translational and rotational degrees of freedom (U_1, U_2, UR_3). This simulates

a rigid support in the physical Shore hardness test. No boundary conditions are applied to the right edge, allowing natural lateral expansion.

Indenter Loading

The indenter is modeled as an analytical rigid surface. A vertical displacement boundary condition ($U_2 = -2.6$ mm) is applied to its reference point, simulating the controlled indentation motion. Horizontal displacement and rotation are fixed ($U_1 = 0$, $UR_3 = 0$).

Displacement control is preferred over force control in this context to avoid numerical instabilities during contact initiation and to ensure consistent simulation behavior across material models. The imposed displacement is sufficient to capture the full indentation response for Shore hardness evaluation.

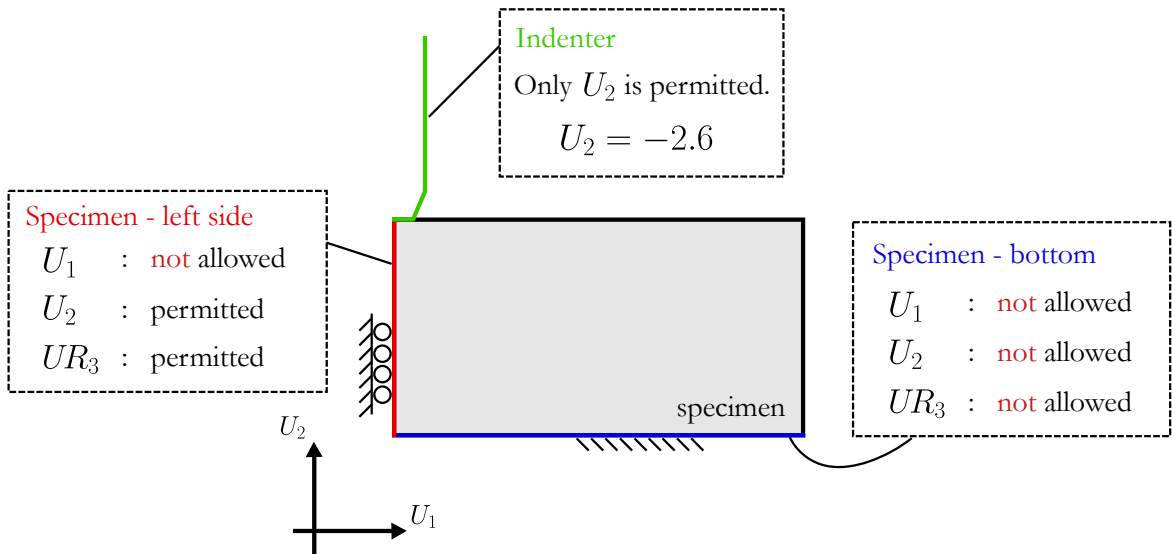


Figure 4.4.1: Boundary conditions applied in the FE model: vertical displacement of the indenter, full constraints at the base, and symmetry conditions on the axis.

4.5 Meshing

A structured meshing strategy was employed to ensure accurate and stable simulation results in the indentation region, while maintaining computational efficiency in the rest of the specimen. The model uses 4-node axisymmetric hybrid elements (CAX4RH), which are ideal for modeling nearly incompressible hyperelastic materials. This element type avoids volumetric locking and is recommended for simulations involving rubber-like behavior. Additionally, 3-node triangular elements (CAX3) were included as backups to ensure successful meshing in partitioned or transition regions.

4.5.1 Mesh Zones and Refinement Strategy

The mesh is divided into three regions based on proximity to the indenter and expected strain gradients. A visually consistent layout of the refinement zones is presented below.

Finest Mesh	Fine Mesh	Regular Mesh
Element size: 0.02 mm This region lies directly beneath the indenter tip. As the indenter geometry is fixed, the deformation remains localized, justifying a constant high-resolution mesh to capture stress gradients accurately.	Element size: 0.05 mm This zone surrounds the finest mesh and extends across 20% of the specimen width. The proportional definition ensures the refinement adapts to specimen geometry while maintaining consistent resolution near the indenter.	Element size: 0.25 mm The remainder of the specimen is meshed more coarsely to reduce computational cost. Since deformation is minimal in this region, the coarser discretization has negligible impact on result accuracy.

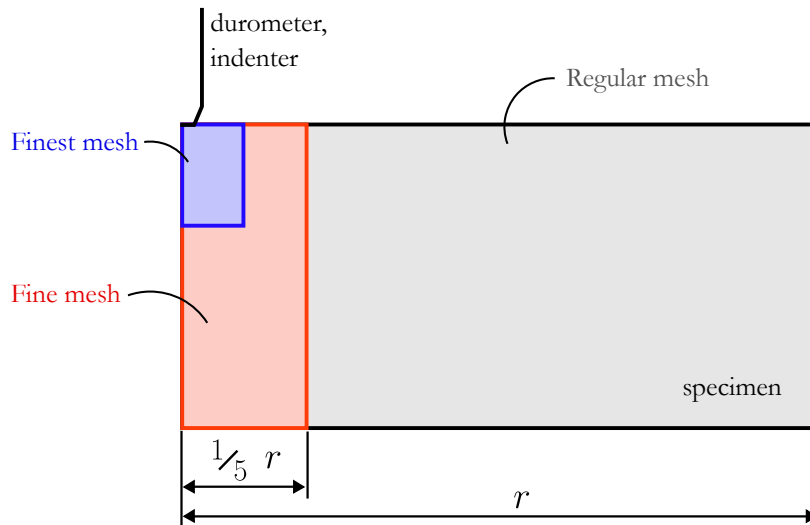


Figure 4.5.1: Different discretization zones in FE model.

Structured quadrilateral elements (CAX4RH) were used throughout to ensure regular alignment with stress gradients, especially under the indenter tip. This layout improves numerical stability and accuracy in the computed force–displacement behavior.

To ensure the reliability and numerical accuracy of the finite element simulations used in Shore A hardness prediction, a focused study was conducted on mesh independence, mesh quality, and solution convergence. These investigations confirm that the simulation outcomes are not artifacts of mesh discretization or numerical instability.

A mesh refinement study was carried out to assess the sensitivity of the Shore A hardness result to mesh resolution. Three mesh configurations were evaluated: coarse, baseline,

and fine. Each model variant used identical geometry, material model (Neo-Hookean), boundary conditions, and indenter loading conditions. Mesh refinement was applied locally, with the finest elements concentrated in the contact region between the indenter and the specimen to accurately capture the deformation behavior and contact mechanics.

Table 4.5.1 summarizes the refinement levels in terms of relative element sizing and total element count.

Table 4.5.1: Mesh refinement levels relative to baseline configuration

Mesh Level	Relative Element Size	Total Elements
Coarse	2.0×	7 891
Baseline	1.00×	31 561
Fine	0.50×	126 241

The Shore A hardness was calculated directly from the simulated force-displacement data using the calibrated spring line of the durometer model. Since this is the primary simulation output, its consistency across mesh refinements serves as a reliable indicator of mesh independence.

The results in Table 4.5.2 show that the computed Shore A values differ by less than 0.1% between the coarsest and finest meshes, indicating excellent convergence and minimal mesh sensitivity. Notably, the baseline mesh yields a hardness of $H_A = 76.60$, with only marginal deviations observed for both coarser and finer configurations.

Table 4.5.2: Hardness results for different mesh refinement levels

Mesh Level	Relative Element Size	Elements	H_A	Relative Difference [%]
Coarse	2.0×	7 891	76.58	0.026
Baseline	1.00×	31 561	76.60	—
Fine	0.50×	126 241	76.54	0.078

These results confirm that the baseline mesh provides sufficient resolution to achieve mesh-independent Shore hardness values, while also offering a favorable balance between computational efficiency and numerical accuracy. It was therefore selected for all subsequent simulations.

The mesh refinement study confirmed that the simulated Shore A hardness values are effectively insensitive to further mesh refinement beyond the baseline configuration. The maximum relative difference between the coarsest and finest meshes remained below 0.1%, indicating excellent mesh independence. Additionally, the mesh quality assessment and convergence behavior analysis validated the numerical stability and reliability of the baseline mesh. Therefore, the baseline mesh was selected for all subsequent simulations as it offers a favorable trade-off between computational cost and result accuracy.

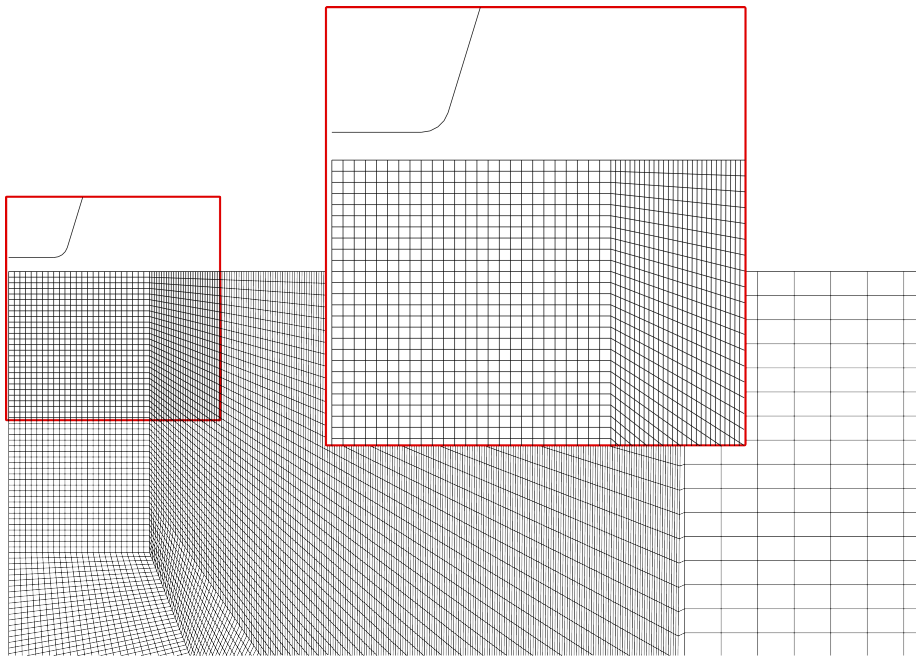


Figure 4.5.2: Specimen meshing in Abaqus.

4.6 Automation of the Simulation

To efficiently evaluate the effects of geometry and material properties on Shore hardness, a fully automated simulation workflow was developed in Abaqus using Python scripting. This system enables batch execution of parameter sweeps across different specimen heights and material models, while ensuring consistency and reproducibility across all simulations.

The automated pipeline starts with defining the input parameters: specimen dimensions, material model type (Neo-Hookean, 1st- or 2nd-order Ogden), and the target range of values for the parametric sweep. Based on these inputs, the script generates a 2D axisymmetric finite element model consisting of the rubber specimen and the rigid Shore durometer indenter. The geometry is partitioned to refine the mesh in critical regions near the contact interface. Material properties are assigned based on the selected constitutive model. The assembly includes surface-to-surface contact with appropriate frictional and normal behavior definitions. Boundary conditions fix the bottom of the specimen and constrain lateral movement, while a prescribed displacement is applied to the indenter reference point.

Each model is meshed using hybrid quadrilateral axisymmetric elements (CAX4RH), and the simulations are executed sequentially across the defined parameter space. After each run, the reaction force and displacement data from the indenter reference node are extracted and saved in CSV format. Post-processing is performed using a separate Python script that filters out pre-contact data, applies the theoretical Shore durometer spring force line, and determines the intersection point with the simulated force–displacement curve. The corresponding indentation depth is converted into a Shore A hardness value, allowing for quantitative comparison across all cases. This automated framework eliminates

manual setup errors, accelerates simulation throughput, and enables scalable studies of Shore hardness under various material and geometric configurations.

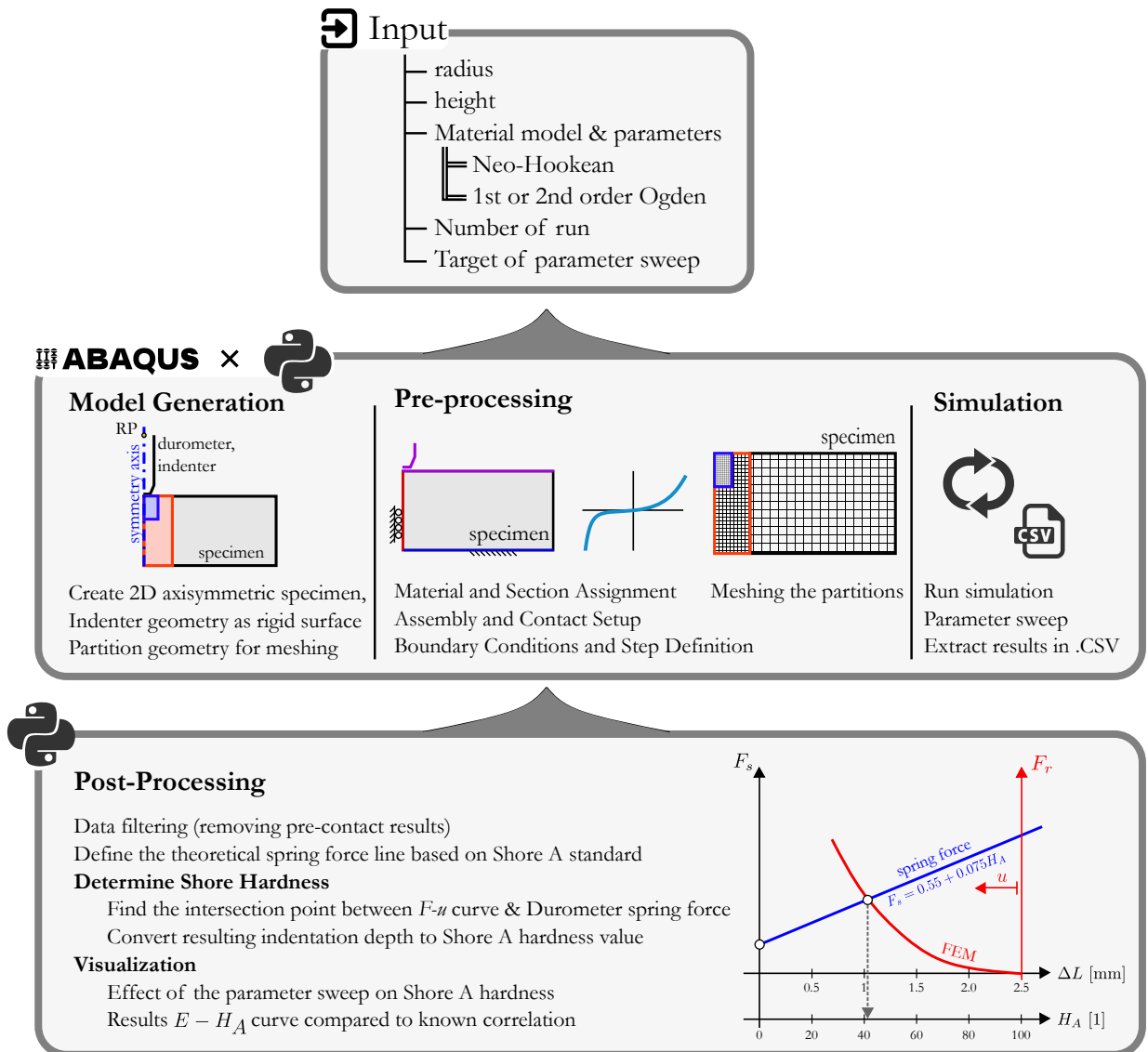


Figure 4.6.1: Automated simulation and post-processing workflow for parametric Shore hardness evaluation.

5

Parameter Study

In this chapter, a systematic parameter study is conducted to investigate how various factors influence the Shore A hardness values derived from finite element simulations. The selection of parameters is primarily guided by the requirements and constraints defined in the Shore hardness testing standard, as well as by practical considerations arising during material model fitting.

Firstly, the effect of geometric parameters is examined. According to the standard, specific requirements must be met regarding the minimum specimen thickness and the distance of the measurement point from any free edge. These constraints translate into two critical geometrical features in the context of the FE model: the specimen width (i.e., the distance to the nearest free edge, related to the indenter's radius) and the specimen height (i.e., the thickness of the specimen). This part of the study aims to reveal how deviations from the ideal geometry influence the computed Shore A hardness values. In addition to simulations, experimental tests with varying specimen geometries are also carried out. While exact numerical agreement between the measured and simulated values is not expected, the comparison aims to validate the simulation results by assessing whether the trends caused by geometrical changes are consistent across both domains.

Secondly, the study explores the influence of material parameters. Since hyperelastic material models often involve multiple non-linear parameters, it is important to assess how sensitive the simulated Shore hardness value is to variations in these model parameters. This analysis provides insight into the robustness of the numerical Shore hardness prediction with respect to uncertainties or variations in material characterization.

Finally, a correction method is proposed for non-standard test setups, where boundary

or geometric constraints cannot fully comply with the prescribed conditions. The goal here is to improve the practical applicability of the simulation approach under real-world conditions.

The typical characteristics of the simulation result shown in Figure 5.1. however the output that is used for later calculation is the reaction force along the y -axis acting on the indenter.

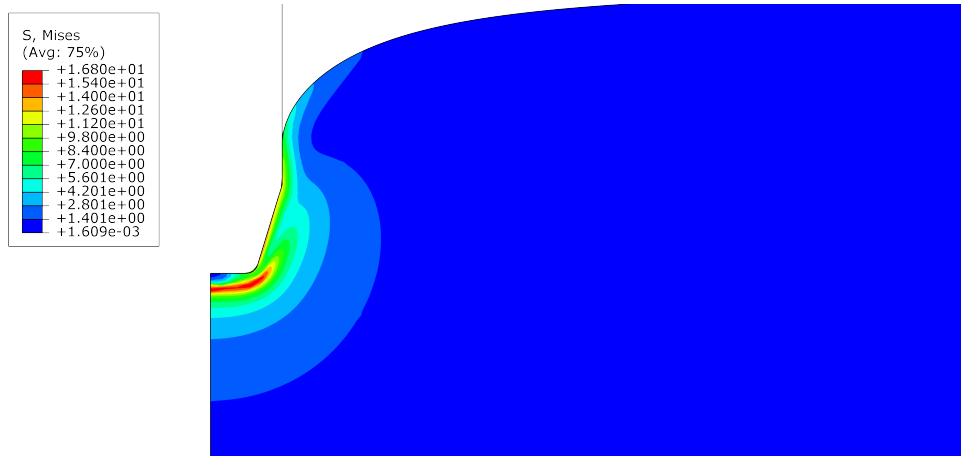


Figure 5.1: Typical characteristics of the simulation result

5.1 Effect of Geometric and Material Parameters

The influence of specimen geometry was investigated by varying both specimen width (radius) and specimen height (thickness). The tested geometries span values below, within, and above the standard-specified dimensions.

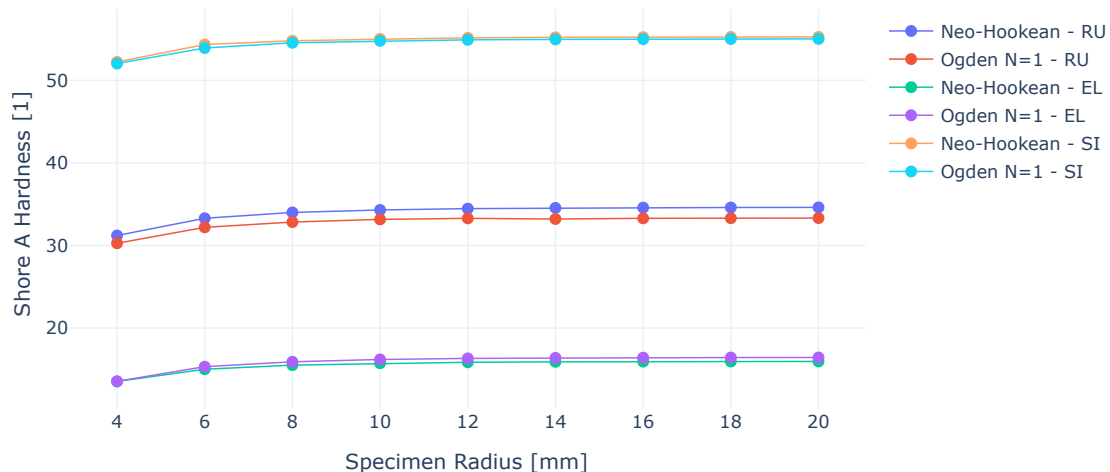


Figure 5.1.1: Shore A hardness vs. specimen width

As seen in Figure 5.1.1, Shore A hardness increases with width and stabilizes beyond a certain threshold. If the specimen radius is below the standard requirement, the Shore A

value is underestimated. This is due to edge effects, where proximity to a free boundary reduces the material's resistance to indentation. The trend is consistent across all six model–material combinations (Neo-Hookean and Ogden N=1 with RU, EL, and SI).

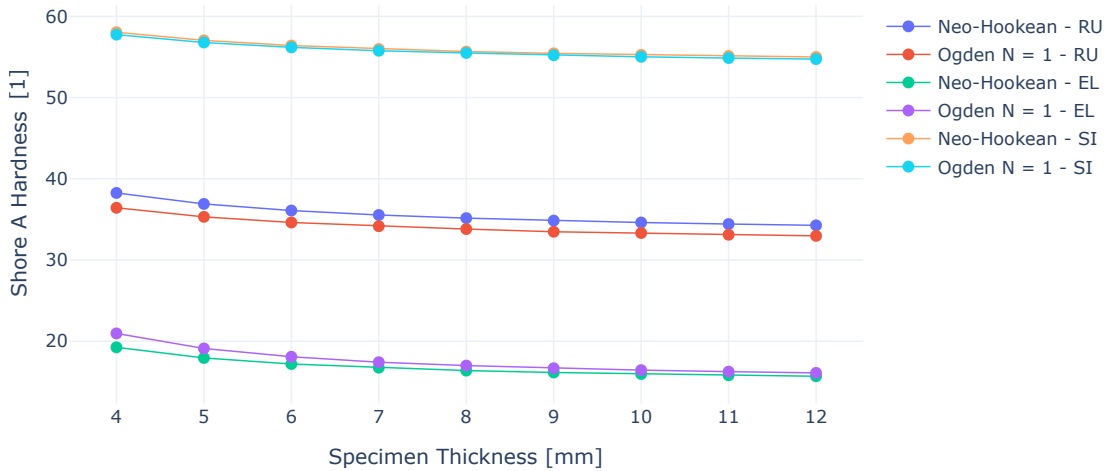


Figure 5.1.2: Shore A hardness vs. specimen height

Figure 5.1.2 shows that insufficient specimen height can lead to overestimated Shore A values. This is caused by interaction with the bottom boundary during indentation, especially if the test is performed on a hard surface such as a table. Beyond 10 mm thickness, the hardness values stabilize.

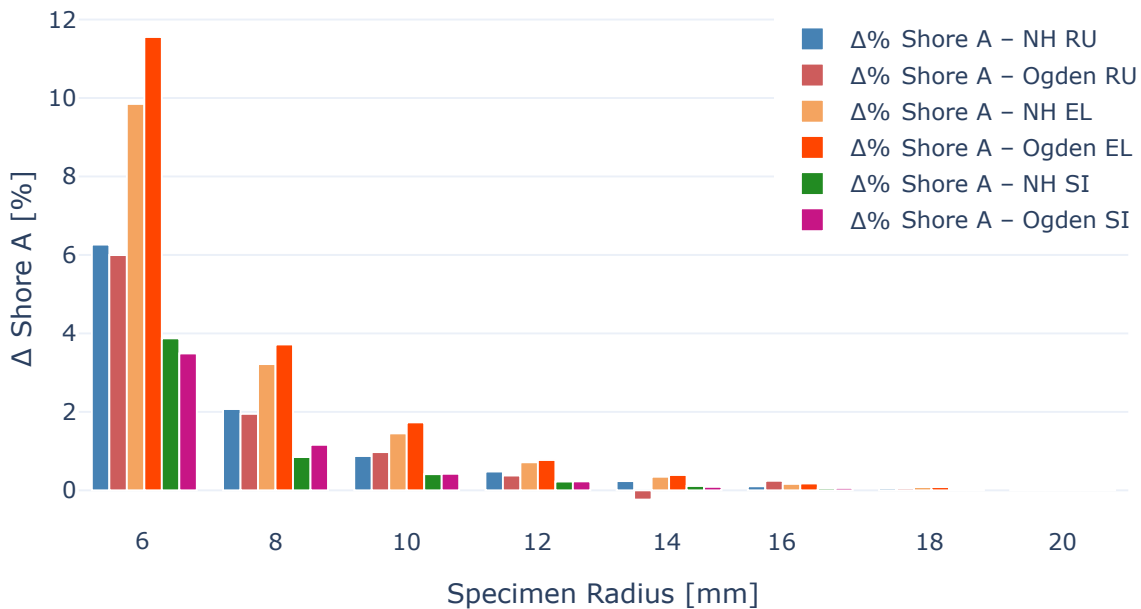


Figure 5.1.3: Relative change in Shore A vs. width

The relative delta plot above shows percentage changes in Shore A hardness. Although the general trend is clear, the relative sensitivity differs between materials. This suggests that a single correction factor may not fully apply across different materials.

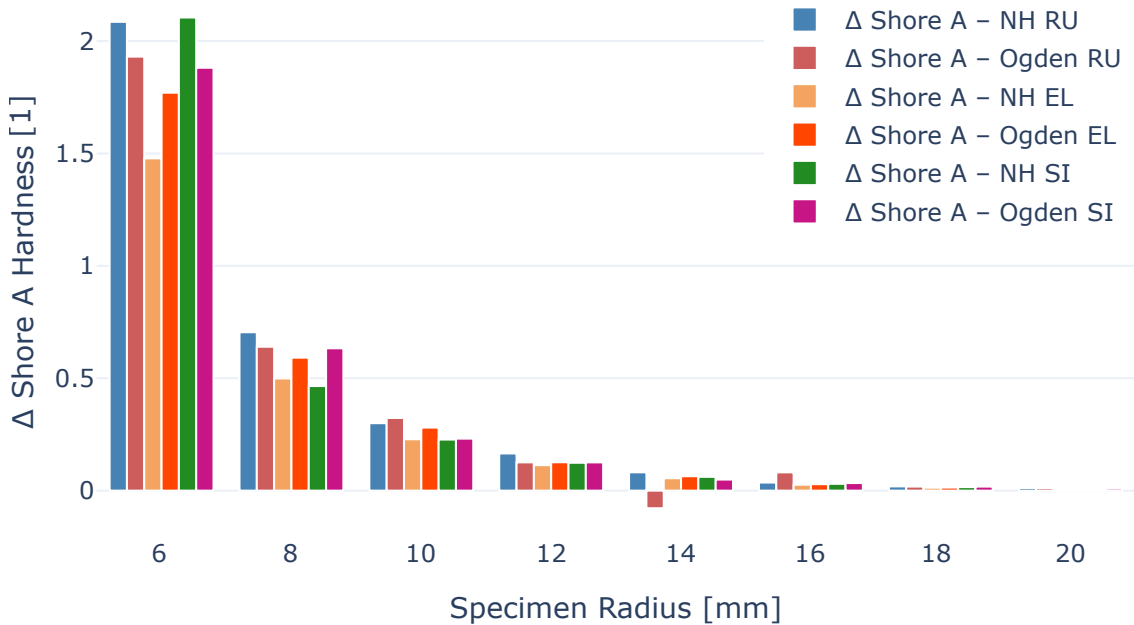


Figure 5.1.4: Absolute change in Shore A vs. width

Interestingly, the absolute delta plot shows more alignment across materials than the relative version. This hints at the possibility of a fixed offset correction being more appropriate than a percentage-based one.

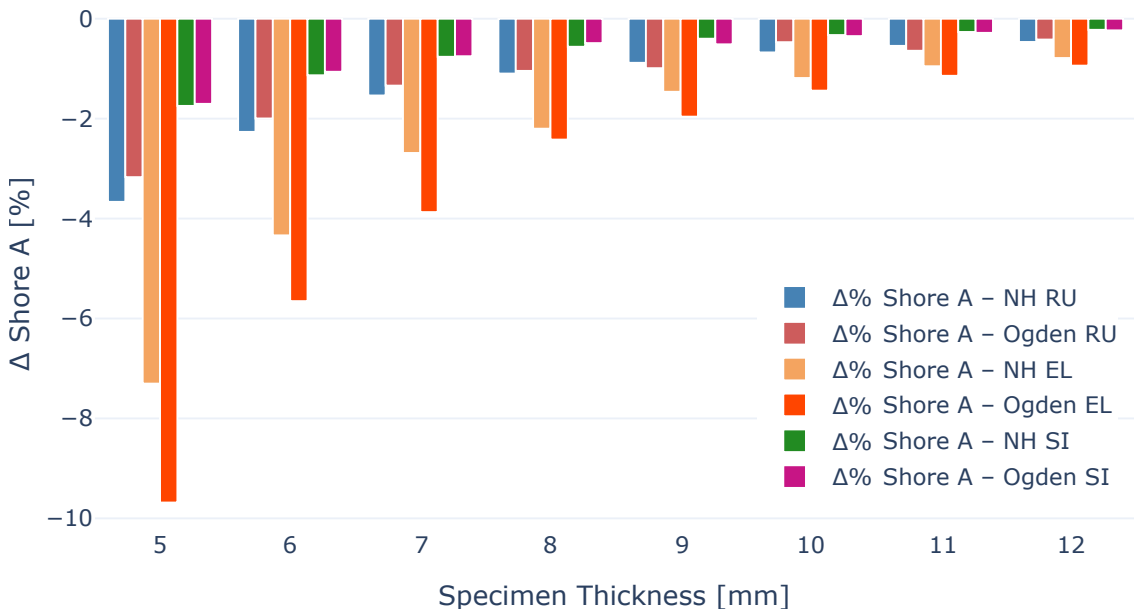


Figure 5.1.5: Relative change in Shore A vs. height

The height-related delta plots show that thin specimens can significantly overestimate hardness due to bottom surface effects. The trend is again material-dependent in relative terms, but more consistent in absolute difference as Figure 5.1.6 shows.

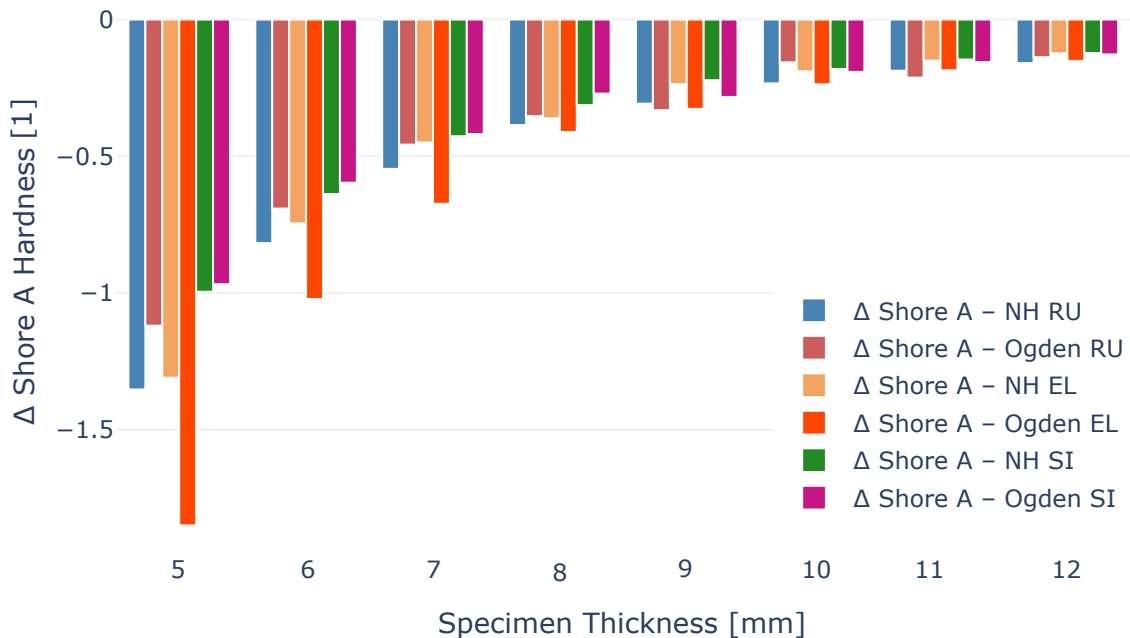


Figure 5.1.6: Absolute change in Shore A vs. height

Each cell in the heatmap of Figure 5.2.4 shows the Shore A hardness for a given radius–thickness combination. The green-framed region denotes the standard-compliant domain. As we move away from this zone, the results visibly diverge: specimens with reduced thickness tend to produce artificially high Shore A results, while extremely small radii underestimate the value.

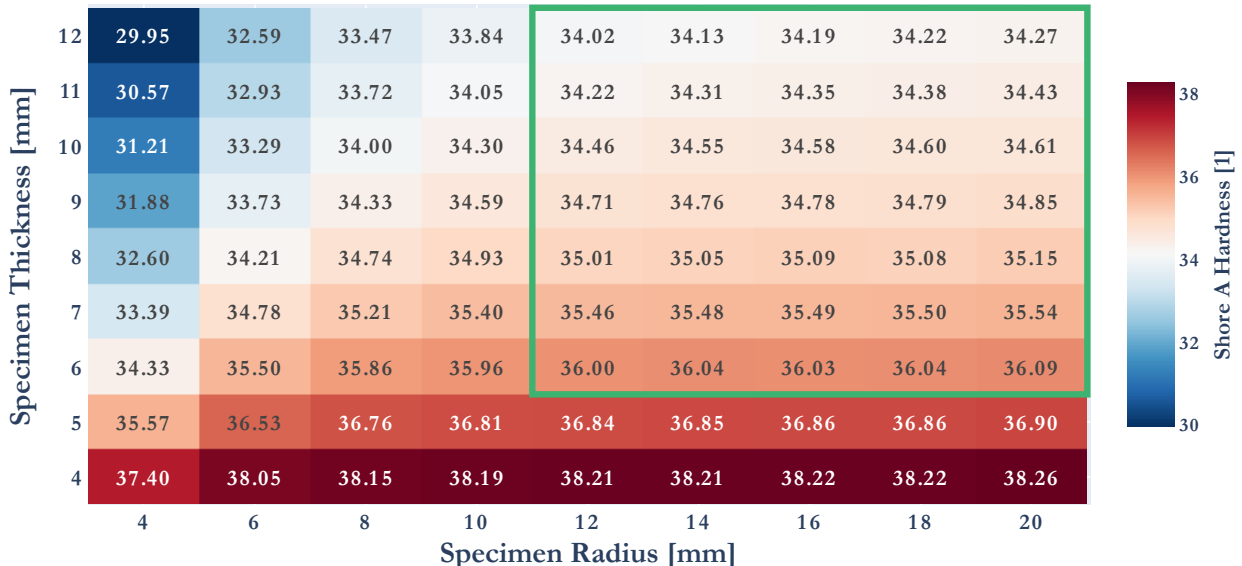


Figure 5.1.7: Shore A values for width and height combinations

The previous figures demonstrated how varying geometrical parameters affect the Shore A hardness for three different materials with distinct elastic modulus. These results indicate that the influence of geometric deviation from the standard is not independent of the material's stiffness. In order to further assess this dependency and to enable the development

of a correction function later on, a reference geometry had to be defined. The chosen reference geometry exceeds the standard's minimum requirements and corresponds to a specimen with dimensions twice the minimum specified values. Using this geometry, Shore A hardness values were simulated for a Neo-Hookean material model by sweeping the C10 parameter from very soft (low C10) to stiffer materials (high C10). The results are shown in Figure 5.1.8.

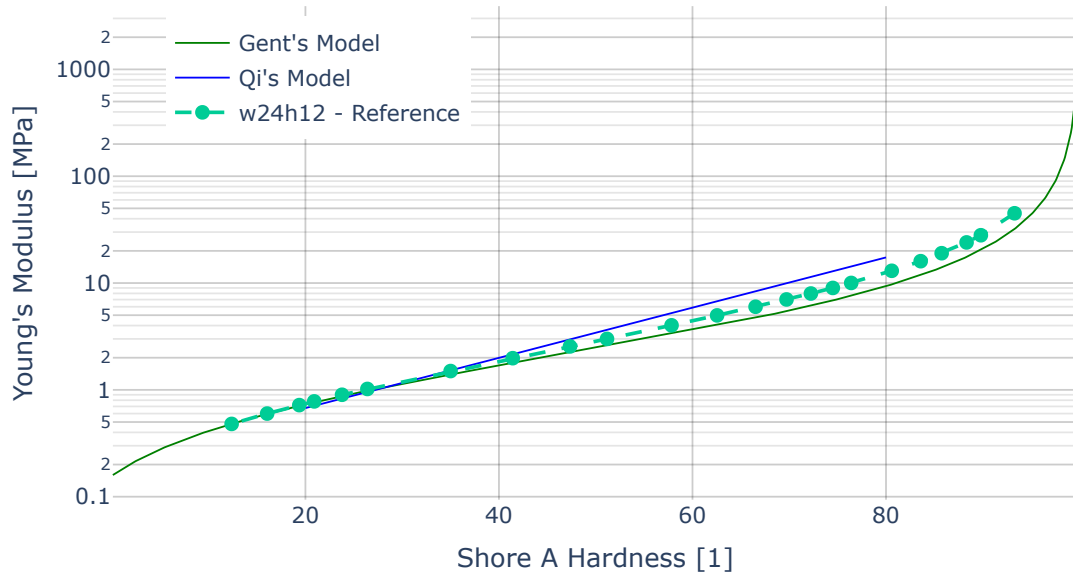


Figure 5.1.8: Reference model compared to Gent's and Qi's models

To analyze geometric sensitivity, four additional configurations were investigated:

- Thickness: 6 mm and 3 mm, with radius fixed at 24 mm.
- Radius: 12 mm and 6 mm, with thickness fixed at 12 mm.

Each configuration used the same set of E values as in the reference case. The resulting Shore A values are compared in Figure 5.1.9.

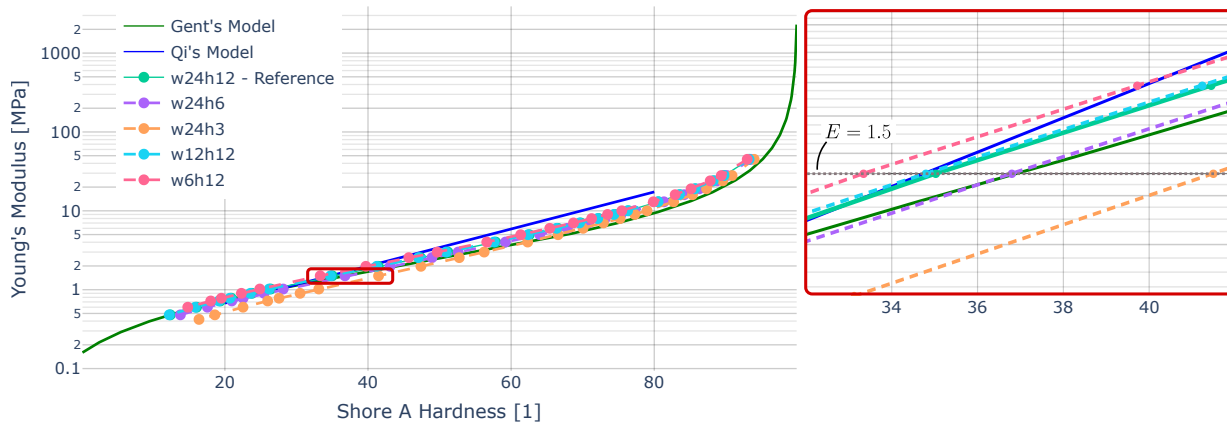


Figure 5.1.9: Comparison of different C_{10} value results for various geometries

Figure 5.1.9 confirms the trends observed earlier: a reduction in radius leads to decreased Shore A values, while a reduction in thickness results in increased values. These effects appear consistent across the entire range of elastic moduli, indicating that the tendency is modulus-independent. However, thickness exerts a stronger influence than width and contributes more significantly to deviations from the reference behavior. Additionally, the distortive effect of substandard geometry diminishes as the elastic modulus increases. To better illustrate this dependency, Figure 5.1.10 presents the relative deviation from the reference model across different geometrical configurations, plotted as a function of Young's modulus.

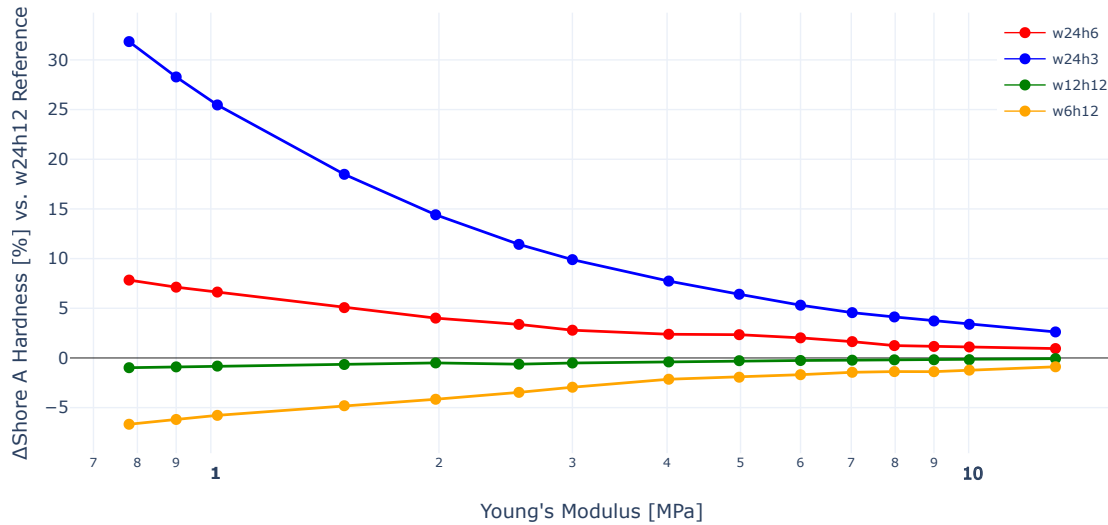


Figure 5.1.10: Effect of geometric distortion relative to the reference model

As seen in Figure 5.1.10, the distorting effect of geometry on Shore A hardness consistently decreases with increasing elastic modulus across all configurations. Importantly, the trend is uniform, reinforcing the idea that a general correction method could be based on geometric and stiffness parameters combined.

Furthermore, the effect of the α_1 parameter in the Ogden model on the resulting Shore A hardness was also investigated. As shown in Figure 5.1.11, α_1 was varied while keeping μ_1 constant. The resulting curve indicates that the relationship between α_1 and Shore A hardness is non-monotonic: initially, increasing α_1 slightly decreases the predicted hardness until a minimum is reached at $\alpha_1 = 1$. Beyond this point, further increases in α_1 result in steadily increasing Shore A hardness values. This behavior highlights the nonlinear sensitivity of the Ogden model to changes in its exponent parameter.

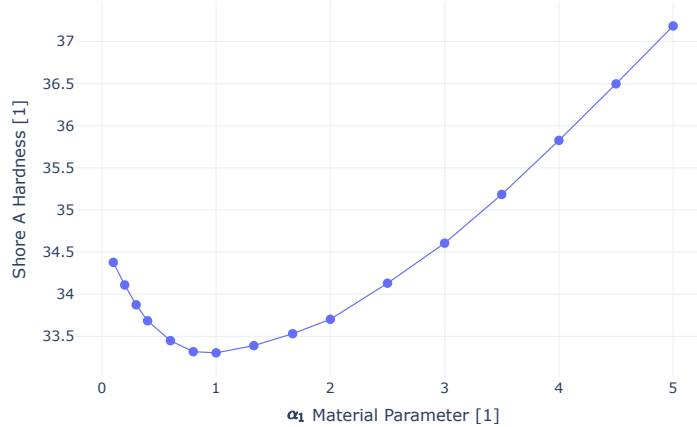


Figure 5.1.11: α_1 parameter effect on Shore A Hardness with a fixed μ_1 value using Ogden N=1

5.2 Correction Method for Non-standard Setups

Based on the diagrams shown in Section 5.1, it can be concluded that any correction for non-standard specimen configurations must depend on multiple parameters. These include the specimen's radius (width), thickness (height), and elastic modulus, as the geometric sensitivity observed is not material-independent. These findings indicate that an effective correction approach must distinguish between the effects of width and thickness and adjust them independently. Based on the result we can state the following about the correction:

- (1) The correction must account for specimen radius, height, and elastic modulus.
- (2) A single-material correction is insufficient; the method must generalize across material parameters.
- (3) The reference geometry should be defined.
- (4) Radius reduction leads to underestimated Shore A values.
- (5) Thickness reduction leads to overestimated Shore A values.
- (6) Thickness has a stronger distorting effect than width.
- (7) Higher elastic modulus reduces the impact of geometric underdimensioning.
- (8) An effective correction must treat width and thickness effects separately and include modulus sensitivity.
- (9) An additive correction seems to be more effective than a multiplicative one.

To determine a correction function that adjusts Shore A hardness values obtained from non-standard geometries, multiple functional forms were tested. The objective was to find a correction term that, when applied, brings the measurements as close as possible to the

reference configuration results. As a starting point, I've defined a correction term in a simple additive formulation as

$$K_A^{\text{sa}} = C_1 \cdot w + C_2 \cdot h + C_3 \cdot E + C_4, \quad (5.2.1)$$

$$H_A^{\text{corr}} = H_A^{\text{orig}} + K_A^{\text{sa}}.$$

The coefficients C_1 to C_4 were tuned with the goal of maximizing the performance of the correction, specifically by bringing the improvement metric (5.2.3) as close to 100% as possible. The quality of any correction function was evaluated using a model-independent improvement metric that compares how much the corrected values reduce the absolute error relative to the original values. Let's introduce the following quantities:

- $H_{i,A}^{\text{ref}}$: Reference Shore A hardness for sample i ;
- $H_{i,A}^{\text{orig}}$: Original simulated Shore A hardness for sample i ;
- $H_{i,A}^{\text{corr}} = H_{i,A}^{\text{orig}} + K_{i,A}^{\text{sa}}$: Corrected Shore A hardness for sample i .

Then, the total absolute error before and after correction become

$$\text{Original: } \sum_i |H_{i,A}^{\text{orig}} - H_{i,A}^{\text{ref}}|, \quad \text{Corrected: } \sum_i |H_{i,A}^{\text{corr}} - H_{i,A}^{\text{ref}}|. \quad (5.2.2)$$

The total improvement in percent is defined as

$$\text{Improvement} := 100 \cdot \left(1 - \frac{\sum_i |H_{i,A}^{\text{corr}} - H_{i,A}^{\text{ref}}|}{\sum_i |H_{i,A}^{\text{orig}} - H_{i,A}^{\text{ref}}|} \right). \quad (5.2.3)$$

The parameter tuning was performed by defining a cost function that returns the negative of the improvement metric, and optimizing this cost using the BFGS algorithm. For each candidate function form, the correction coefficients were iteratively adjusted to minimize the total absolute deviation between corrected values and their reference counterparts. To ensure fair comparison across materials and geometries, each sample from a non-standard setup was matched to the closest reference result based on elastic modulus, using a nearest-neighbor search. Furthermore, to avoid the effects of nonlinear behavior at the extremes, the optimization process was restricted to data within the Shore A range of [20, 80]. Outside this interval, the correlation between Shore A hardness and elastic modulus becomes highly nonlinear and less generalizable. In this additive form, the best total improvement achieved was 70.24%. While this is a promising result, it was not yet sufficient. Therefore, a multiplicative variant of the same linear correction was evaluated as

$$K_A^{\text{sm}} = C_1 \cdot w + C_2 \cdot h + C_3 \cdot E + C_4, \quad (5.2.4)$$

$$H_A^{\text{corr}} = H_A^{\text{orig}} \cdot K_A^{\text{sm}}.$$

This approach yielded a lower performance of only 55.47% improvement, likely due to

instability or sign changes in the multiplicative scaling term. Guided by the observations summarized earlier in List 1, a more sophisticated correction function was constructed as

$$K_A^{\text{cm}} = C_1 \cdot E + C_2 \cdot \frac{1}{w} + C_3 \cdot \frac{1}{h} + \log(E) \left(C_4 + C_5 \cdot \frac{1}{h} + C_6 \cdot \frac{1}{w} \right) + C_7, \quad (5.2.5)$$

$$H_A^{\text{corr}} = H_A^{\text{meas}} \cdot K_A^{\text{cm}}.$$

This formulation led to a significantly better alignment between the corrected and reference results, reaching a total improvement of 88.62% in the [20, 80] Shore A range. To further explore this structure, I also implemented an additive variant of the same more complex function as

$$K_A^{\text{ca}} = C_1 \cdot E + C_2 \cdot \frac{1}{w} + C_3 \cdot \frac{1}{h} + \log(E) \left(C_4 + C_5 \cdot \frac{1}{h} + C_6 \cdot \frac{1}{w} \right) + C_7, \quad (5.2.6)$$

$$H_A^{\text{corr}} = H_A^{\text{meas}} + K_A^{\text{ca}}.$$

With this formulation, I was able to reach a total improvement of 91.37% in the [20, 80] Shore A range.

H_A	Mean difference from the reference [%]				
	original	K_A^{sa}	K_A^{sm}	K_A^{ca}	K_A^{cm}
12-95	6.78	2.73	4.62	1.05	1.46
20-80	6.23	1.85	2.77	0.54	0.71
Before correction			After correction		

Table 5.2.1: Mean difference from the reference for different models.

Based on these results showed in Table 5.2.1, the additive correction model K_A^{ca} was selected for further use, as it delivered the best overall performance. The final fitted coefficients of the correction can be seen below.

$$\begin{aligned} K_A^{\text{ca}} \text{ Coefficients: } & C_1 = 0.0522, \quad C_2 = 10.3625, \quad C_3 = -26.2376, \\ & C_4 = -1.0419, \quad C_5 = 7.3570, \quad C_6 = -0.0607, \quad C_7 = 1.9575. \end{aligned}$$

The resulting coefficients support the earlier hypotheses summarized in List 1. Notably, the coefficient associated with specimen thickness is larger in magnitude than the one for width, confirming that thickness has a stronger influence on Shore A distortion. To evaluate how well the correction function compensates for deviations caused by non-standard geometries, the results were compared against the reference configuration. Figure 5.2.1 presents the updated version of the earlier geometry comparison (Figure 5.1.10), now showing the residuals after correction has been applied.

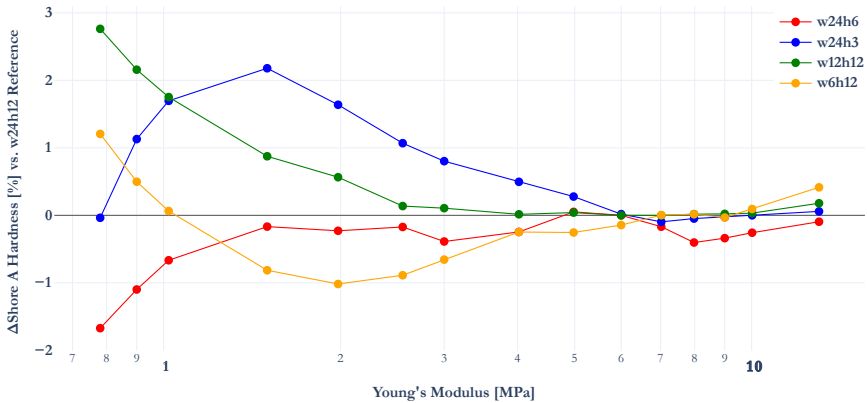


Figure 5.2.1: Deviation from the reference model after correction

Further analysis of the correction function's performance is provided in Figures 5.2.2 and 5.2.3, which display the residual error relative to the reference both in absolute and percentage form. Figure 5.2.2 shows the absolute difference in Shore A hardness between the corrected values and the matched reference points. The deviations remain within approximately ± 1 hardness unit across the full modulus range, indicating that the correction remains stable and effective regardless of stiffness.

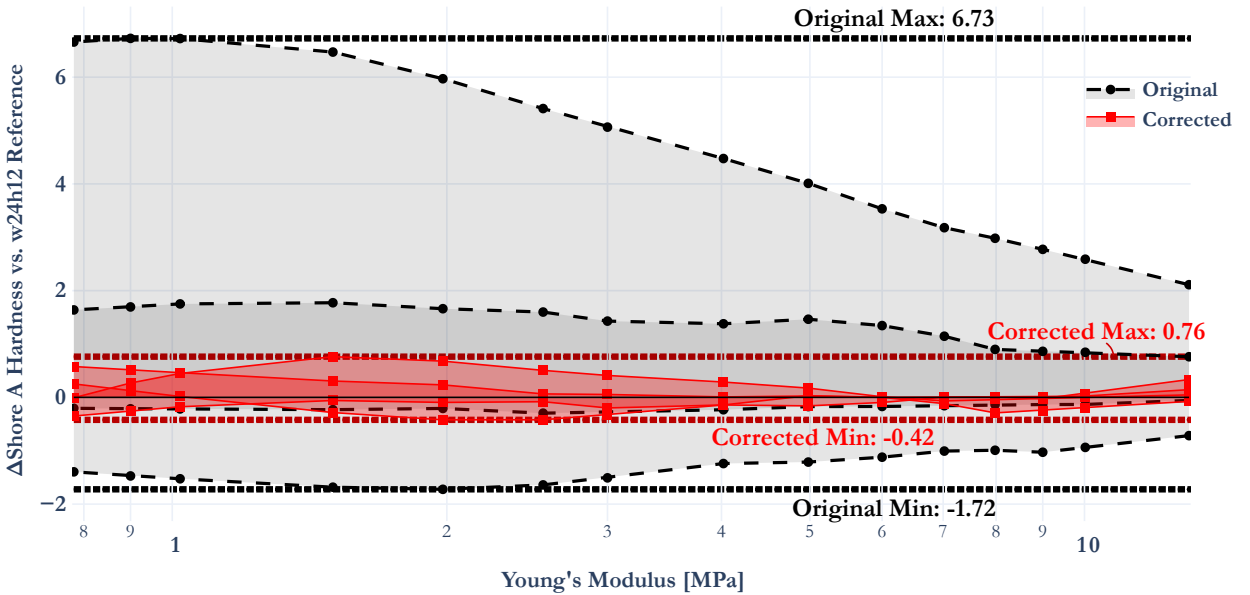


Figure 5.2.2: Absolute deviation from the reference after correction

Figure 5.2.3 expresses the same results as percentage deviation. This view is particularly informative in the low-modulus range, where even small absolute differences can translate to large relative errors. In the uncorrected case, errors reached up to 32%, while after applying the correction, residuals were reduced to within $\pm 3\%$. This confirms the model's effectiveness not only in absolute terms but also in maintaining relative accuracy. It is worth noting that percentage-based plots can exaggerate error where reference values are low. Therefore, using both absolute and relative views provides a more complete picture. While the absolute view is useful for evaluating engineering impact, the percentage view highlights proportional consistency across the material range.

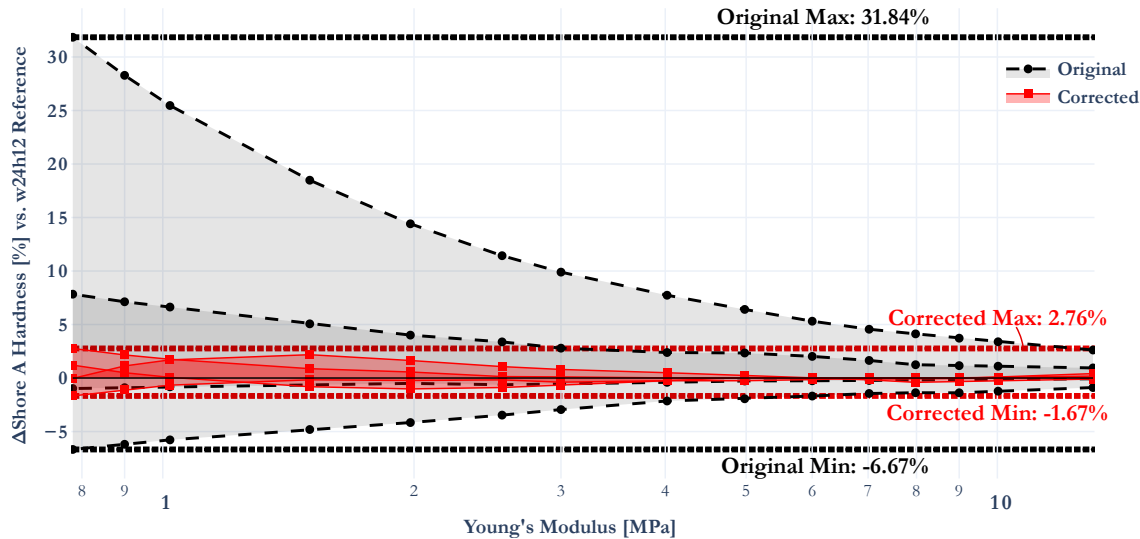


Figure 5.2.3: Percentage deviation from the reference after correction

To visualize how the correction performs across the entire geometric domain, Figure 5.2.4 presents the corrected Shore A hardness values as a heatmap. This figure includes all evaluated geometry combinations, but only those outside the standard reference dimensions were actually subjected to correction. The reference geometry zone defined as radius ≥ 12 mm and thickness ≥ 6 mm remained unchanged by design.

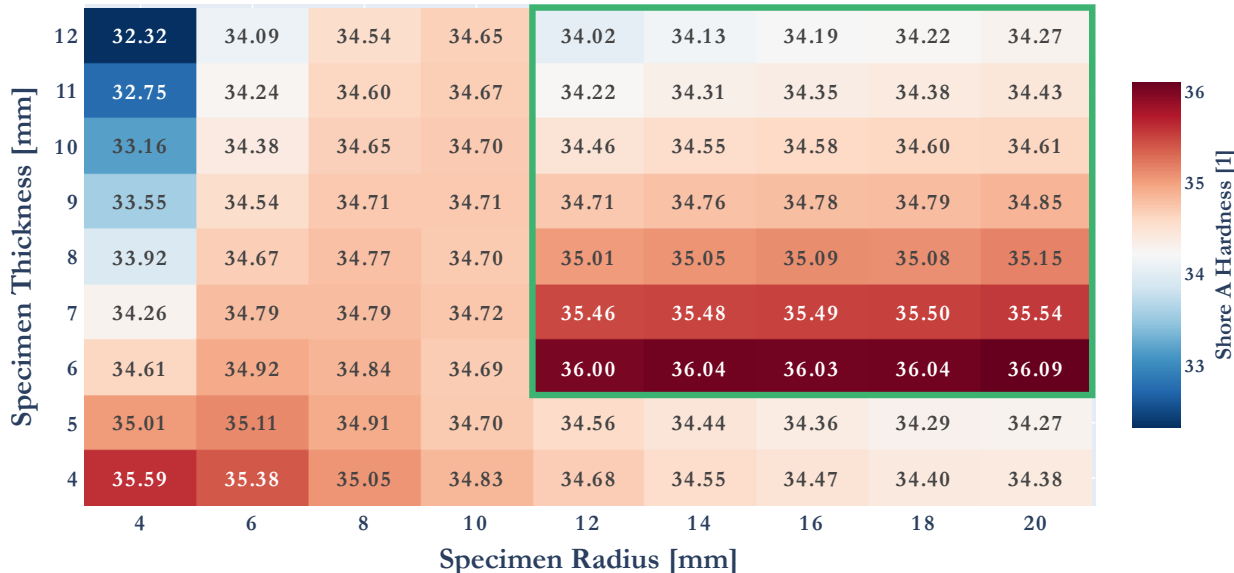


Figure 5.2.4: Shore A values for width and height combinations after correction

To better assess the benefit of the correction, Figure 5.2.5 shows a side-by-side comparison of the original and corrected Shore A values. This visualization emphasizes the convergence of the corrected values toward the reference range, especially in configurations with smaller radii or reduced thickness, where geometric distortion was previously significant.

To quantitatively evaluate the correction's effect, the statistical dispersion of Shore A

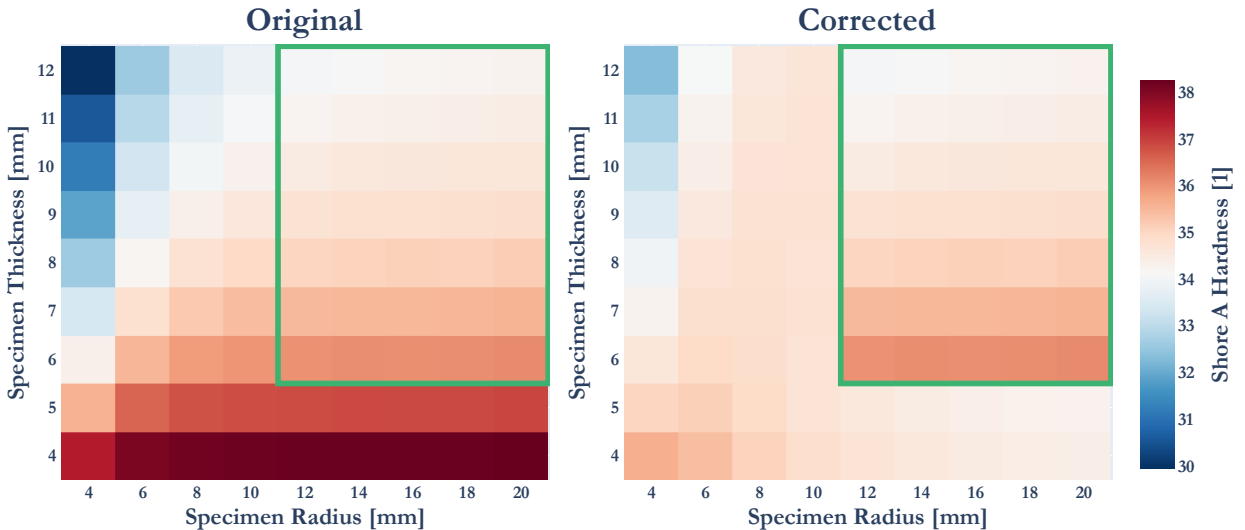


Figure 5.2.5: Comparison of original and corrected Shore A values for different geometry

values was analyzed within and outside the standard geometry zone. The standard deviation was calculated using the `STDEV.S` function in Excel, applied separately to the raw and corrected data outside the reference dimensions.

Prior to correction, the standard deviation in the non-standard zone was $s_{\text{before}} = 2.19$, compared to $s_{\text{ref}} = 0.63$ in the reference zone. This indicates significant variability due to geometric distortion. After applying the correction, the standard deviation in the non-standard region dropped to $s_{\text{corr}} = 0.59$, demonstrating that the correction not only reduces the mean deviation from the reference but also substantially suppresses the variance among the affected configurations.

The sample standard deviation s for a dataset $\{x_1, x_2, \dots, x_n\}$ is calculated as

$$s = \sqrt{\frac{1}{n-1} \sum_{i=1}^n (x_i - \bar{x})^2},$$

where \bar{x} is the sample mean. The fact that $s_{\text{corr}} < s_{\text{ref}}$ suggests that the correction not only aligns the values but also homogenizes the response across different geometries. These results reinforce the effectiveness of the chosen correction model both in reducing systematic error and improving consistency across non-standard geometries.

6

Experimental Results and Validation

6.1 Introduction

The previous chapter introduced a correction method and evaluated its effectiveness based on simulation results. However in engineering practice, the theoretical conclusions must be validated through physical experiments. To confidently assert the reliability of the proposed method, experimental validation is a must. The validation strategy is based on the following considerations.

First, experimental data must include measurements performed on test specimens made from the same material but with varying geometries. These geometries should include a reference configuration that satisfies the standard requirements, as well as under-dimensioned configurations that deviate from the standard ideally similarly to those used in the simulations.

Second, if the experimental results show the same trends in Shore A hardness as observed in the simulation plots (Figure 5.1.1 and Figure 5.1.2), then the initial assumptions summarized in Table 1 can be considered valid.

Finally, if applying the additive correction function to experimental results—computed relative to the measured reference values—produces outcomes that align with the corrected behavior shown in Figure 5.2.3, then the correction method can be considered practically applicable. While further validation on a larger dataset would improve confidence, for the purposes of this thesis, the correction will be tested on specimens made from three different materials and geometries, selected to represent a range of deviations from the standard.

The test specimens used in the experimental validation are shown in Figure 6.1.1. The figure displays specimens fabricated from three distinct materials: Silicone (white), Rubber (red), and Elastosil (pink). These physical specimens were used for Shore A hardness measurements under varied geometric configurations.



Figure 6.1.1: Specimens used for validation. Colors: Silicone (white), Rubber (red), Elastosil (pink).

Table 6.1.1 summarizes the measurement configurations and results obtained from the specimens shown in Figure 6.1.1. For each material and geometry, the table includes the measured Shore A hardness, the corrected values using the additive method, standard deviations, and the absolute percentage deviation from the respective reference measurement.

Material	E [MPa]	Thickness [mm]	Width [mm]	Shore A Hardness Meas	Shore A Hardness Corr	St. Dev	Abs. mean diff. Meas [%]	Abs. mean diff. Corr [%]
Rubber	1.35	14	24	37.50		0.66		
		9	24	38.64	38.15	0.76	3.04	1.75
		5	24	39.91	37.18	0.85	6.43	0.86
		14	12	36.90	37.85	0.67	1.60	0.93
		14	6	36.45	38.26	0.72	2.80	2.03
Silicone	6.17	15	24	61.82		0.72		
		10	24	62.21	63.97	0.97	0.63	0.38
		5	24	63.5	63.25	0.88	2.70	0.75
		15	12	62.76	63.71	0.74	1.52	0.79
		15	6	62.41	64.22	1.32	2.07	0.77
Elastosil	0.43	12	24	27.89		0.73		
		6	24	30.20	28.17	0.64	8.28	1.01
		3	24	33.01	26.16	0.60	18.36	6.22
		12	12	27.96	28.78	0.61	0.25	3.18
		12	6	27.47	29.15	0.55	1.51	4.53

Table 6.1.1: Summary of test specimens used for experimental validation. Reference specimens are highlighted per material type.

The results in Table 6.1.1 are visualized in Figures 6.1.2, 6.1.3, and 6.1.4, which show the overall effect of the applied additive correction across all measured configurations, including variations in both thickness and width. These plots clearly demonstrate that the correction method reduces the deviation caused by undersized geometries.

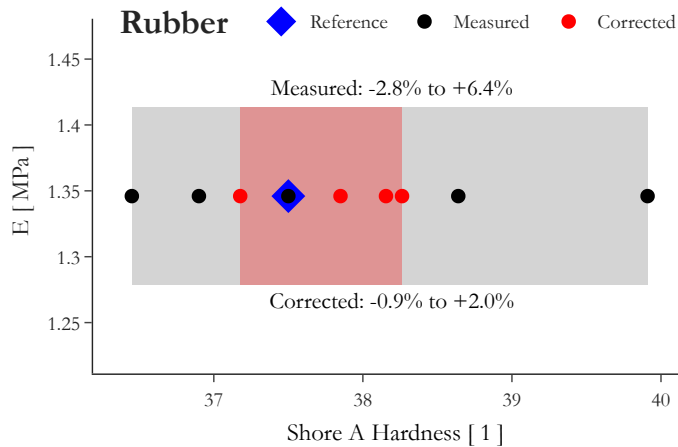


Figure 6.1.2: Effect of correction across all geometries for Rubber specimens.

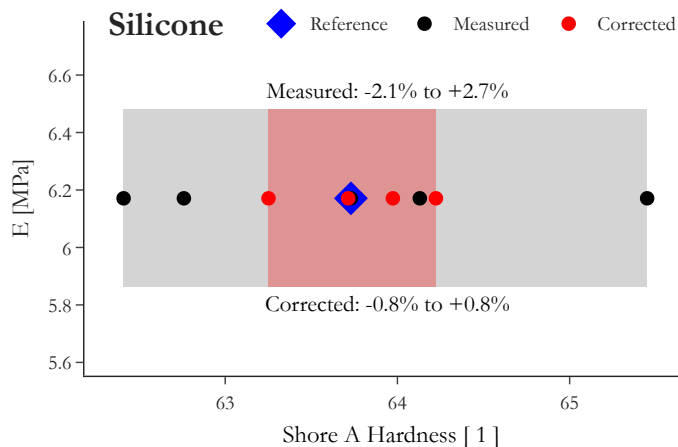


Figure 6.1.3: Effect of correction across all geometries for Silicone specimens.

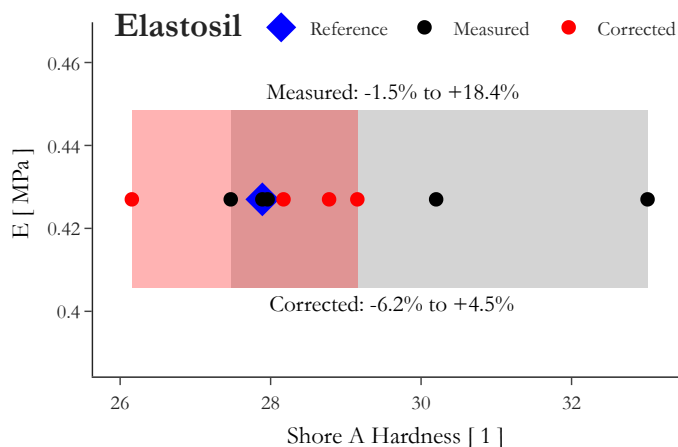


Figure 6.1.4: Effect of correction across all geometries for Elastosil specimens.

Figures 6.1.5, 6.1.6, and 6.1.7 show the results for specimens where only the thickness varied and the width remained constant. In these cases, the corrected values align more closely with the reference.

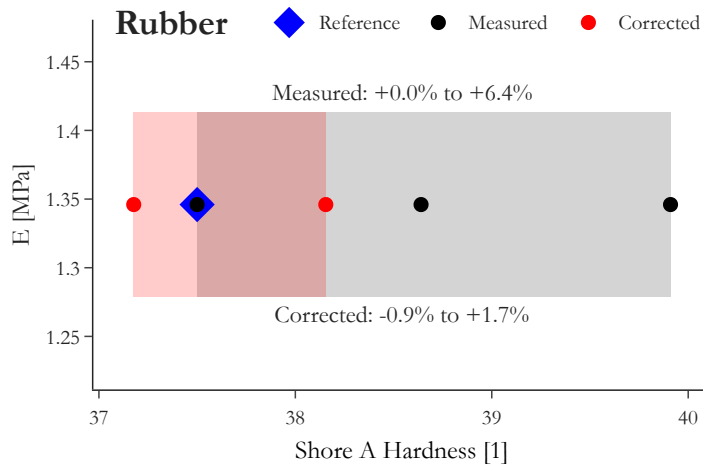


Figure 6.1.5: Effect of correction across all geometries for Rubber specimens.

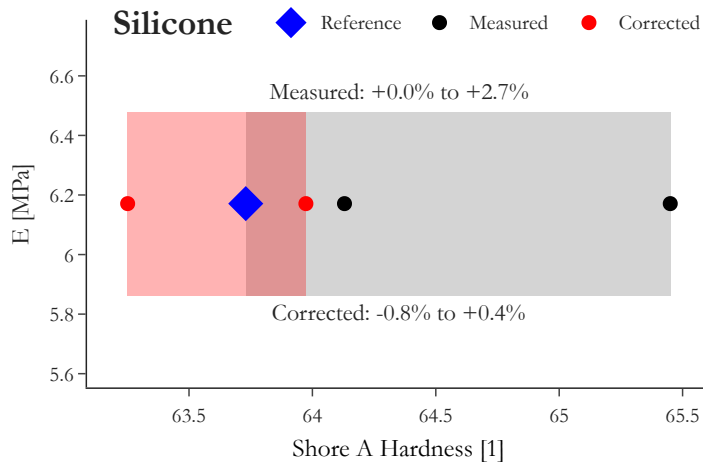


Figure 6.1.6: Effect of correction across all geometries for Silicone specimens.

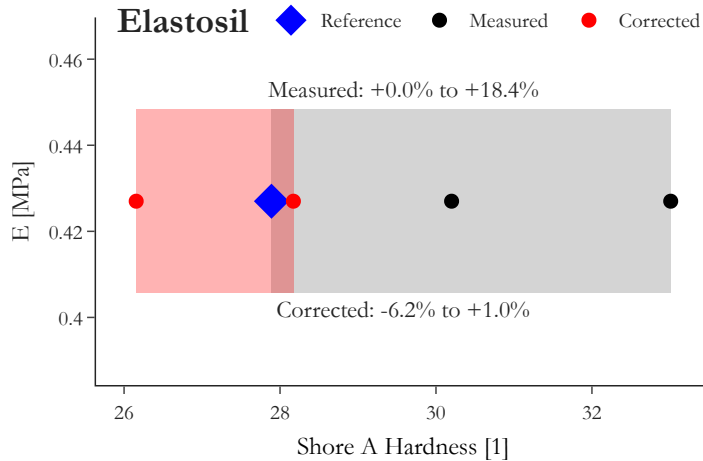


Figure 6.1.7: Effect of correction across all geometries for Elastosil specimens.

In contrast, the correction is less effective when compensating for deviations in width. This may be due to the practical challenges associated with measuring very narrow specimens, where the likelihood of user-induced measurement error increases.

Before correction, the average deviation from the reference across all three materials was 4.1%. After applying the correction, this was reduced to 1.87%, indicating an average improvement of 2.24 percentage points. When considering only the reference and thickness-varied specimens, the average deviation dropped from 6.57% to 1.83%, resulting in a 4.74 percentage point improvement on the given data due to the correction model.

Finally, the simulation results are compared against the experimental measurements. As described in Chapter 3, three different materials were tested (Elastosil, Rubber, and Silicone). The corresponding material parameters which is determined from the measurements described in Section 4 are summarized in Tables 3.3.1, 3.3.2, and 3.3.3 for multiple material model. Using the simulation method presented in this thesis, Shore A hardness values can be computed and compared with the experimentally obtained values. The comparison between simulated and measured hardness is shown in Table 6.1.2.

Table 6.1.2: Comparison of simulated and measured Shore A hardness values

Material	h [mm]	w [mm]	Measured H_A	Simulated H_A	Relative Difference [%]
Rubber	14	24	37.50	32.90	12.3
	9	24	38.64	33.64	12.9
	14	12	36.90	32.58	11.7
	14	6	36.45	30.93	15.1
Silicone	15	24	61.20	61.30	-0.2
	10	24	62.05	61.56	0.8
	5	24	63.49	62.85	1.0
	15	12	61.50	61.16	0.6
	15	6	61.16	59.86	2.1
Elastosil	12	24	27.89	16.11	42.2
	6	24	30.20	18.09	40.1
	3	24	33.01	24.59	25.5
	12	12	27.96	15.91	43.1
	12	6	27.47	14.68	46.6

As for the Silicone across all tested specimen geometries, the simulated Shore A hardness values match the measured values with high accuracy. This demonstrates that, when the material model parameters are well-identified and the test data is reliable, the simulation method presented in this thesis can reproduce real-world behavior. The Silicone results provide validation for the overall simulation and material modeling framework. In contrast, for both the Elastosil and Rubber materials, the simulation results deviate noticeably from the measured Shore A hardness values. In the case of Elastosil, the limited surface quality

likely contributed to increased measurement uncertainty. As for the Rubber material, it was cut from a pre-deformed, curved commercial product, which made it difficult to prepare flat and uniform test specimens.

Based on these findings, it can be concluded that while the current simulation method can produce accurate Shore A hardness predictions, however further experimental measurements are recommended with softer materials to strengthen the validation of the model. The results observed for the Silicone material nonetheless demonstrates that the simulation results can be brought into alignment with reality when the material model parameters are well-identified and the input data is reliable. There is also a small but consistent difference in the results for specimens with narrower widths. This is mainly due to the difference in boundary conditions. In the simulations, the bottom edge of the specimen is completely fixed. In real measurements, however, the edges can slightly lift off the surface because of the way the device presses on the material. Additionally since we are packing the specimens onto each other the alignment uncertainties can also influence the measured values for narrow specimens.

In conclusion, the correction method developed in this thesis reliably reduces the error introduced by non-standard geometry, and in particular, it performs well in compensating for distortions caused by reduced specimen thickness. However, expanding the measurement dataset would be a valuable step toward more confident and generalizable model validation.

7

Summary

The objective of this thesis was to gain a comprehensive understanding of Shore A hardness testing for soft polymer materials, with particular focus on the influence of specimen geometry and material parameters on the measured hardness value. The study was carried out through several hundred finite element simulations conducted in the Abaqus environment. These simulations were automated with a Python script, which handled model generation, meshing, assignment of hyperelastic material models (Neo-Hookean and Ogden), definition of boundary conditions, execution of the simulations, and post-processing. The Shore A hardness was computed by locating the intersection of the simulated reaction force curve and the calibrated spring force line of the durometer.

The parametric study primarily focused on the specimen's geometrical parameters, namely width and height. To isolate the effect of geometry, the simulations were carried out using fixed material models with multiple discrete values of Young's modulus. The results showed that the influence of geometry is not independent of material stiffness, for low-modulus materials ($E < 7 \text{ MPa}$) and small specimen heights ($h < 6 \text{ mm}$), a significant deviation in the computed Shore A hardness was observed compared to standard geometry.

Based on the simulation data, two types of correction models were developed, multiplicative and additive functions, each fitted to account for the effects of specimen width, height, and Young's modulus. These models aim to reduce the error introduced when testing non-standard geometries. The correction functions were validated against experimental measurements, which confirmed the trends observed in the simulations and consistently yielded hardness values closer to the standard reference. However, the measurements also highlighted the limitations of the correction approach due to measurement uncertainties

and additional unmodeled factors.

Further improvement may be achieved by incorporating IRHD hardness testing and employing the Coupled Eulerian–Lagrangian (CEL) simulation technique, which allows for more accurate modeling of large deformations and material flow. Additionally, alternative mathematical forms for the correction function (e.g., sigmoid or hybrid models) may offer better generalization across wider parameter ranges. Quantitative evaluation of these approaches remains a subject for future work.

Összefoglaló

A diplomamunkám célja az volt, hogy átfogó módon megismerhessem a lágy polimer anyagok Shore A keménységvizsgálatát, valamint azt, hogy milyen geometriai és anyag-paraméterek befolyásolják a mérőműszerről leolvasható eredményt. A munka során több száz végeselemes szimulációt végeztem el Abaqus környezetben, amelyeket egy automatizált Python szkript generált, futtatott és értékelt ki éjszakákon átvélen. Ez a szkript elvégezte a testek modellezését, hálózását, anyagtulajdonságainak megadását (Neo-Hooke és Ogden modellek), a peremfeltételek definiálását, a szimulációk futtatását, valamint az eredmények kiértékelését és a szükséges utómunkákat is, beleértve a Shore A keménység kiszámítását a rugóerő - reakcióerő függvények metszéspontja alapján.

A paraméter vizsgálatok során főként a geometriai paraméterekre koncentráltam különböző rugalmassági modulusszal rendelkező anyagokra vonatkozóan, ahol a próbatest szélességét és magasságát változtattam. Ezen szimulációk során ugyanazon anyagmodellt használva több diszkrét rugalmassági modulusnak megfelelő anyagparaméterrel vizsgáltam a geometriai méretek hatását. Az így kapott keménységrétekek alapján arra jutottam, hogy a geometria befolyása nem független az anyag rugalmassági modulusától: különösen kis merevségű ($E < 7 \text{ MPa}$) anyagok és kis magasságú próbatestek ($h < 6 \text{ mm}$) esetén tapasztalható jelentős eltérés a mért keménységen.

A szimulációs eredmények alapján 2-2 multiplikatív és additív korrekciós függvényt illesztettem, amely a Young-modulus, a próbatest szélessége és magassága alapján próbálja korrigálni a nem szabványos geometriák esetén mért Shore A keménység értékeit. A korrekciós modell hatékonyságát laboratóriumi mérésekkel is ellenőriztem, amelyek igazolták a tendencia helyességét továbbá minden esetben egy, a referenciahoz jobban közelítő eredményt adott a korrekció. Továbbá azonban a mérési eredmények rámutattak arra is, hogy a mérési bizonytalanságok és más, nem modellezett hatások korlátozzák a korrekciós eljárás pontosságát.

A diplomamunkám során alkalmazott módszerek és a levont következtetések alapot adnak a további fejlesztésekre. Az áthatóbb vizsgálat érdekében érdemes alkalmazni az IRHD keménységvizsgálatot, valamint a Coupled Eulerian-Lagrangian (CEL) szimulációs megközelítést, amely többek között folytonos anyagátmenetek kezelését teszi lehetővé.

Bibliography

- [1] American Society for Testing and Materials. ASTM D2240: Standard Test Method for Rubber Property - Durometer Hardness.
- [2] American Society for Testing and Materials. ASTM D1415: Standard Test Method for Rubber Property - International Hardness
- [3] International Organization for Standardization. ISO 48-1: Rubber, vulcanized or thermoplastic - Determination of hardness
- [4] Ulrich Blobner. 1915- 2015: 100 Years of Shore A Hardness Testing A historical review of the development and research of the Shore A measuring method with reference to today's testing practice, O-Ring Prüflabor Richter [Online]
- [5] H. J. Qi, K. Joyce, M. C. Boyce. Durometer hardness and the stress-strain behaviour of elastomeric materials. *Rubber Chemistry and Technology*, 76(2), 419–435, 2003 [Online]
- [6] A. N. Gent. On the relation between indentation hardness and Young's modulus, *Institution of Rubber Industry - Transactions*, 34, 46–57, 1958
- [7] Meththananda IM, Parker S, Patel MP, Braden M. The relationship between Shore hardness of elastomeric dental materials and Young's modulus. *Dent Mater*. 2009
- [8] Abaqus Documentation: Theory manual [Online]
- [9] M. J. Lohr, G. P. Sugerman, S. Kakaletsis, E. Lejeune, M. K. Rausch. An introduction to the Ogden model in biomechanics: benefits, implementation tools and limitations. *Philosophical Transactions of the Royal Society A*, 380(2220), 2022. [Online]
- [10] Mitutoyo - User's manual for hardmatic HH-300 series [Online]